2021

Quantifying Shape of Star-Like Objects Using Shape Curves and A New Compactness Measure

Gopal K. Mulukutla
University of New Hampshire, Durham, gopal.mulukutla@unh.edu

Emese Hadnagy
University of New Haven, ehadnagy@newhaven.edu

Matthew Fearon
U.S. Naval Research Laboratory, matthew.fearon.ctr@nrlmry.navy.mil

Edward Garboczi
National Institute of Standards and Technology, edward.garboczi@nist.gov

Quantifying Shape of Star-Like Objects Using *Shape Curves* And A New Compactness Measure

Gopal K. Mulukutla[1], **Emese Hadnagy**[2], **Matthew G. Fearon**[3] and **Edward J. Garboczi**[4]

[1.] Earth Systems Research Center, University of New Hampshire, 12 College Road, Durham, NH 03824, USA. gopal.mulukutla@unh.edu

[2.] Department of Civil and Environmental Engineering, University of New Haven, 300 Boston Post Rd, West Haven, CT 06516, USA.

[3.] NRC Fellow, National Academy of Sciences at U.S. Naval Research Laboratory, 7 Grace Hopper Ave, Monterey, CA 93943, USA

4. National Institute of Standards and Technology, 325 Broadway MS647, Boulder, CO 80305

Abstract

Shape is an important indicator of the physical and chemical behavior of natural and engineered particulate materials (e.g., sediment, sand, rock, volcanic ash). It directly or indirectly affects numerous microscopic and macroscopic geologic, environmental and engineering processes. Due to the complex, highly irregular shapes found in particulate materials, there is a perennial need for quantitative shape descriptions. We developed a new characterization method (*shape curve* analysis) and a new quantitative measure (c*ompactness,* not the topological mathematical definition) by applying a fundamental principle that the geometric anisotropy of an object is a unique signature of its internal spatial distribution of matter. We show that this method is applicable to "star-like" particles, a broad mathematical definition of shape fulfilled by most natural and engineered particulate materials. This new method and measure are designed to be mathematically intermediate between simple parameters like sphericity and full 3D shape descriptions.

For a "star-like" object discretized as a polyhedron made of surface planar elements, each s*hape curve* describes the distribution of elemental surface area or volume. Using several thousand regular and highly irregular 3-D shape representations, built from model or real particles, we demonstrate that s*hape curves* accurately encode geometric anisotropy by mapping surface area and volume information onto a pair of dimensionless 2-D curves. Each shape curve produces an intrinsic property (length of shape curve) that is used to describe a new definition of *compactness*, a property shown to be independent of translation, rotation, and scale. *Compactness* exhibits unique values for distinct shapes and is insensitive to changes in measurement resolution and noise. With increasing ability to rapidly capture digital representations of highly irregular 3-D shapes, this work provides a new quantitative shape measure for direct comparison of shape across classes of particulate materials.

Keywords: star-like shapes, characterization of shape, shape curves, compactness

1.0 Introduction

Shape is an important consideration in the study of natural and processed particulate materials. Shape influences numerous microscale and macroscale processes and it is important in understanding many chemical, physical, and biological properties in numerous areas of the science and engineering of particulate materials (Riley et al. 2003; Chung et al. 2010; Albanese et al. 2012). For example, volcanological processes dictate the shape and size of particles emitted from volcanic eruptions, which makes shape an important indicator of the fate and extent of transport of volcanic clouds (Rose and Durant 2009, 2011). Shape is also a key factor in understanding fluid drag in the motion of suspended non-spherical particles (Leith 1987; Loth 2008; Bagheri and Bonadonna 2016). By implication, better characterization of particle shape can improve understanding of a wide range of processes and the behavior of numerous natural and synthetic materials (Bullard and Garboczi 2013).

Particulate materials contain complex morphological features over multiple length scales (relative to some measure of overall object size). Their shape can range from smooth, mildly aspherical forms to angular particles observed in engineering or environmental systems (Connolly et al. 2020) to highly porous and fractalesque geometries seen in volcanic ash (Bagheri et al. 2015). The morphological features of such materials can be classified into a three-tiered hierarchy based on observational scale. At the largest scale, *form* describes closeness to an ideal shape, curvature of the overall form (*roundness)* describes an intermediate scale property, while surface texture (*asperity*) describes small length-scale geometric properties (Barrett 1980; Blott and Pye 2008).

There are two broad classes of quantitative shape measures developed for particulate materials – single factor and parametric measures (Jia and Garboczi 2016). For example, Corey shape factor (CSF) is a single factor measure developed from three measurable sizes of a particle

in mutually-perpendicular directions: the longest dimension (d_{max}), the shortest dimension (d_{min}), and an intermediate or medium direction (d_{med}) (Loth 2008), and defined as,

$$\mathrm{CSF} = \frac{d_{min}}{\sqrt{d_{max}\, d_{med}}} \qquad (1)$$

Practical considerations and design of measurements limit many single factor shape measures to target one or two of the length scale hierarchies. The CSF parameter was originally described using data captured by mechanical sieving (Corey 1949), and subsequently used with caliper measurements and microscopic images (Komar and Reimers 1978). For particulate materials, by using a limited number of size measurements, CSF bypasses complexities in surface texture to get a snapshot of shape expressed in large and intermediate scale features. Another single factor shape measure is the classic Wadell *sphericity* (Ψ), which gives a measure of the ratio of the surface area of a sphere with the same volume to the surface area of the particle (Wadell 1932):

$$\Psi = \frac{\pi^{\frac{1}{3}}\,(6\,V)^{\frac{2}{3}}}{\mathrm{A}} \qquad (2)$$

where A and V are particle surface area and volume, respectively.

While *sphericity* is a more widely used measure, CSF has been shown to be more suited to characterize shape when the goal was to understand fluid drag coefficients of angular particles (Loth 2008). This is likely because three size measurements capture "local" changes better in these materials. More "global" measurements like volume and surface area do not capture the complex arrangement of mass within a particle. The terms "local" and "global" here describe surface features with a single particle as reference.

However, CSF is known to be less sensitive to equidimensional regular shapes, with a cube and a sphere producing similar values (Connolly et al. 2020). Similarly, *sphericity* is affected by ambiguous values in a broader range. For example, the *sphericity* of most ellipsoidal shapes can

vary approximately in the range of 0.3 and 1.0. The approximate range for most commonly-encountered cylinders (0.45- 0.87), objects perceived to be entirely different in shape, also fall within this range (Li et al. 2012). As a result, more complete shape description is often performed by combining single parameter measures with material-specific terms that provide a better visual understanding of shape. For example, descriptive terminology is commonly used to describe the shape of volcanic ash using terms such as *vesicular*, *angular*, *blocky*, *twisted*, and *elongated droplets with smooth* or *fluidal surfaces* (Heiken 1972). While there exists a range of descriptive features for rocks and other geological materials (Blott and Pye 2008), there is no standard terminology for qualitative shape description across material classes (Jia and Garboczi 2016).

Parametric series measures, on the other hand, are more complex as they capture shape information as a series of curves representing the shape profile of particles. Often, these representations are encoded using complex Fourier series and they can be developed from 2-D or 3-D form outlines of most particle shapes. Various approaches exist for the development of these measures, such as the Fourier descriptors approach for 2-D and 3-D outlines (Boon et al. 1982; Bowman et al. 2001; Mollon and Zhao 2013, 2014) and a Fourier series based 2-D approach (Barclay and Buckingham 2009). Another related approach uses spherical harmonic (SH) analysis applied to star-shaped particles (Garboczi 2002; Chung et al. 2010). Parametric series measures can capture subtle features in particles and have unique advantages in applications related to shape reconstruction and representation. Single parameter measures, however, typically find specific applications in shape-property studies.

These factors underscore the need for continuing research towards developing fully quantitative shape measures applicable to all irregularly shaped objects, something that was highlighted almost two decades ago (Taylor 2002). The overarching objective of this work is the development of a shape measure that aligns with single parameter measures but uses the power of parametric series measures to accurately capture scale-specific shape information for shape

classification in order to have better discrimination between dissimilar shapes between classes. If successful, the shape measure will be in a mathematical sense intermediate: more complex than simple parameters but not as complex as parametric series. The rest of this paper is divided into sections detailing theory behind a new approach to shape classification (shape curve theory) and its application on regular and Euclidean shapes(Section 2). In section 3 we develop a shape classification approach and extend shape curve theory with a case study on irregularly shaped particles. Section 4 discusses considerations in the application of shape curve analysis including factors like invariances and measurement sensitivities, followed by a summary of the method and important conclusions (Section 5).

2.0 Background and Methods

2.1 Star-like shapes

The "star-like" description of a three-dimensional object *S* is a mathematical definition that is fulfilled if there exists an interior point *O* in *S* such that the line segment connecting *O* to any point *p* on the surface of S lies entirely in the interior of S (Dorf and Hall 2003; Garboczi and Bullard 2017). This feature has also been described as the object being "devoid of non-intersecting" surfaces or having a single-valued surface (Barclay and Buckingham 2009; Mulukutla et al. 2017). A particle being "star-like" is a weaker condition than convexity, although if a particle is "star-like" it can be proved that there exists a convex subset of the star-like particle so that the particle is star-like with respect to any point *O* in this convex subset (Smith 1968). This weaker condition allows a wider variety of shapes to conform to this property than only those that are convex. All regular and irregular convex shapes are also star-like, as well as particles with minor concavities such as those derived from geological materials (e.g., sand, rock, gravel, volcanic ash, powders) and most particles made from industrial processes, assuming interior pores are neglected (Bullard and Garboczi 2013; Mollon and Zhao 2013; Qian et al. 2016). We describe a particle as being "star-shaped" if it meets

the mathematical definition of "star-like." Only particles that are at least star-shaped are investigated in this work.

2.2 Shape Curve Theory for Convex Objects

Consider a sphere (a regular convex and thus star-like shape) discretized by closed differential elements, so constructed that their appropriate integral produces the surface area or volume of the shape. A closed differential element for volume would be a spherical sector consisting of a spherical cap and a right circular cone (Figure 1a). The same spherical sector can also be considered a closed surface area differential element by discounting the surface area of the conical portion of the spherical sector, as the surface area of the conical element does not contribute to the surface area of the sphere. A similar construction of closed differential elements for a prolate and oblate spheroids and right circular cylinders are constructed (Figure 1 b-d). Specifically, for prolate and oblate spheroids the closed differential elements are so chosen that they align with the major axis and minor axis, respectively, and allow a circular base for the spheroidal cap and simpler formulations for the surface area and volume.

For a sphere of radius *r* with a spherical sector element, given the height of the spherical cap is *h*, and the sphere radius is *r*, the volume of the spherical cap may be written as

$$\mathrm{V}_{\mathrm{cap}}=\frac{\pi}{3}h^2(3r-h) \qquad (3)$$

The volume of the right circular cone portion of the spherical sector is

$$\mathrm{V}_{\mathrm{cone}}=\frac{\pi}{3}r^2(2hr-h^2) \qquad (4)$$

The spherical sector volume can then be written as

$$V=\frac{\pi}{3}h^2(3r-h)+\frac{\pi}{3}r^2(2hr-h^2) \qquad (5)$$

Similarly, the surface area of a spherical sector (excluding the surface area of the cone) can be written as

$$A=2\pi rh \qquad (6)$$

In order to understand the distribution of space within the sphere and its relationship to the expression of shape, we use the concept of solid angle. By definition, the solid angle (Ω) of any object subtended at an arbitrary point O located at distance r is given as $\Omega = \frac{A}{r^2}$ (units: *steradians*), where A is the spherical surface area that the object projects onto a unit sphere centered on the arbitrary point (Taylor and Thompson 2008). Solid angle provides a measure of the extent an object's projection covers the unit circle. The solid angle of the spherical sector subtended at sphere center O is the same as the solid angle of the spherical cap. This can be assumed to be equal to the solid angle of a circular disk formed by the base of the spherical cap. Because the closest circular section of the spherical cap subtends the largest projected area on a unit sphere located at O, all other projections of the spherical cap will be obscured by this area. As a result, the solid angle of the spherical sector (Ω) can be given by the solid angle of a thin circular disk (Asvestas and Englund 1994).

$$\Omega_{cap} = 2\pi\,(1 - \cos\theta_c) \qquad (7)$$

where $\theta_c = tan^{-1}\left(\frac{\sqrt{2rh-h^2}}{r-h}\right)$ is the angle between the axis and the straight line that connects the center and any point on the circular base. A set of similar underlying equations of surface area and volume for the non-spherical shapes considered here (spheroids and right circular cylinders) are summarized in Table 1.

The total solid angle subtended at the center for any star-like shape is 4π. This result has been illustrated using numerical examples (Mulukutla et al. 2017). It can also be proven mathematically, as summarized in section S1 (supporting information). This intrinsic property allows the definition the *physical fraction of an object* (Δ)(Mulukutla et al. 2017), a function describing the physical extent of an object in terms of the solid angle it subtends divided by 4π.

$$\Delta(\Omega) = \frac{\Omega}{4\pi} \quad , \qquad 0 \leq \Delta \leq 1 \qquad (8)$$

To capture shape information from the entire sphere, we initially consider a hemisphere and build a sequence of spherical caps that progressively integrates surface area and volume at each step. The analysis can then just be doubled to reflect the whole shape. Each spherical cap encompasses the area and volume of the previous element, making them inherently cumulative and integrative of shape information captured within. Equations (5) to (8) and the cumulative solid angle and physical fraction for the whole sphere can be rewritten in a normalized numeric form as

$$V_n = \frac{2}{V}\left(\frac{\pi}{3}{h_n}^2(3r - h_n) + \frac{\pi}{3}r^2\left(2h_n r - {h_n}^2\right)\right) \qquad (9)$$

$$A_n = \frac{2}{A}(2\pi r h_n) \qquad (10)$$

$$\Omega_n = 2\left(\frac{\mathrm{A}_n}{r^2}\right) \qquad (12)$$

$$\Delta_n = 2\left(\frac{\Omega_n}{4\pi}\right),\ 0 \le \Delta \le 1\text{, where } \Omega_n = 2\left(2\pi\,(1 - \cos\theta_c^n)\right) \qquad (13)$$

where V and A are the volume and surface area of the whole sphere, respectively. The variable $h_n = nr$, $n = 0, \frac{1}{N}, \frac{2}{N}, \ldots 1$, where N is the number of steps (or number of spherical sector elements) considered for the sphere.

We define s*hape curves* as a pair of curves that describe the variation of the *cumulative surface area fraction function* (CSAF) and the *cumulative volume fraction function* (CVF) with the *cumulative physical fraction function* (CPF). For star-like shapes, we define the *cumulative physical fraction function* (*CPF*, Δ^c) as a continuous distribution that progressively depicts the *fraction of an object.* Since Eqs (9)-(13) integrate information from the previous element, a simple extraction of data will provide a series of discrete cumulative data:

$$\Delta^c = \{\Delta_1, \Delta_2, \Delta_3 \ldots \Delta_n\} \qquad (14a)$$

Similarly, the cumulative series for surface area ($CSAF$, $A^C; 0 \leq A^C \leq 1$) and volume (CVF, $V^C; 0 \leq V^C \leq 1$) are defined as:

$$A^C = \{\mathrm{A}_1, A_2, A_3 \dots A_n\} \qquad (14b)$$

$$V^C = \{\mathrm{V}_1, V_2, V_3 \dots V_n\} \qquad (14c)$$

Analysis was performed by discretizing one half the axis of symmetry of each shape by 1000 differential elements and the surface area and volume shape curve data doubled to reflect the behavior of the entire object. Shape curves were generated for spheres, prolate and oblate spheroids, and right circular cylinders using the exact mathematical formulations described in Eqs (9) to (14) and in Table 1. Aspect ratios in the range 1 to 100 were examined for each shape. We define aspect ratio (≥ 1) as c/a for prolate spheroid, a/c for oblate spheroid, where a and c are the semi-axes. For a right circular cylinder, aspect ratio is defined as L/R_c, where L is the height and R_c the radius. Illustrative shape curves for prolate spheroids and right circular cylinders along with spheres are shown in Figure 2. Shape curves for a sphere (aspect ratio = 1), being an equi-dimensional shape, are marked by a straight line. They show that aspect ratio differentiates shapes, with increasing length of curves for increasing values. Shape curves of right circular cylinders are each marked by a sharp linear segment. This is a result of the planar face of a cylinder contributing to a substantial portion of the solid angle. With increasing aspect ratio, the planar face of the right circular cylinder becomes increasingly distant from the center of the cylinder, thus contributing a smaller solid angle fraction. This shows that *shape curves* capture intrinsic signatures of convex objects. In order for shape curve theory to apply to irregular shapes, there is a need to examine its validity for star-like shapes.

2.3 Properties of Shape Curves

Shape curves provide a non-dimensional method to understand the inherent relationship between an object's surface area and volume integrated over the entire surface of the object. While

there exists a power-law scaling for the surface area to volume relationship for Euclidean shapes (Bullard and Garboczi 2013), *shape curves* can quantify these differences in a non-dimensional way. For a given volume, an isoperimetric inequality states that a spherical shape has the smallest surface area (Pólya and Szegö 1951). This pattern is captured in the linear behavior of the sphere shape curves. Any change from a sphere to a different shape (e.g. into an ellipsoid) leads to a higher surface area, a different volume, and an observable change in shape curve signatures. These changes can be captured in the length of the shape curves, which can be determined by summing the length of individual segments formed by Eqs14a-c. In the case of a sphere, each shape curve is a 45° straight line with bounds [0 1] on each axis. The length of such a straight-line segment is easily calculated:

$$(l_s, l_v)_{sphere} = \sqrt{2} = 1.4142 \qquad (15)$$

where l_s and l_v refer to the length of the surface area and the volume shape curves, respectively.

The definition of a new parameter that we call compactness (C) is derived by normalizing the object's *shape curve* lengths to those of a sphere:

$$C = \left(\frac{l_s}{\sqrt{2}}, \frac{l_v}{\sqrt{2}}\right) \qquad (16)$$

We denote these normalized shape curve lengths as:

$$C = (L_s, L_v) \qquad (17)$$

Compactness by the way of normalized shape curve lengths provide a two-component measure describing the shape of an object relative to a sphere, with each component integrating independent information that comes from the particle shape. This metric is different from the usual topological measure, also called compactness, which is a measure of the nature of a point set (Bribiesca 2008). For our case, the compactness of a sphere is exactly:

$$C = (1, 1) \tag{18}$$

Plots in Figures 3a-b capture compactness values (shape curve lengths) for spheroids and right circular cylinders. Increasing aspect ratio results in increasing shape curve lengths. For the same aspect ratio and value of a, volume shape curve lengths of prolate and oblate spheroids are identical (due to equal volume), but surface area shape curve lengths are distinct. In subsequent sections, we use shape curve theory to further explore properties of star-like shapes using numerical representations of regular and irregular shapes and to develop a basis for shape classification.

2.4 Shape Curves from Numerical Representations of Star-like Objects

Many imaging and reconstruction techniques are available to capture object shapes with scales ranging from nanometers to millimeters and meters (Gualda et al. 2010). These include X-ray computed tomography (XCT) based measurements of internal structures and external surfaces (Garboczi 2002; Pirard 2012; Vonlanthen et al. 2015), stereology-based techniques developed from 2-D XCT to aid 3D reconstructions (Proussevitch et al. 2007), 2-D surface imaging techniques combined with 3D reconstruction using scanning electron microscopy (SEM) (Tafti et al. 2015), and stereographic-SEM based reconstruction of partial surfaces of objects (Colucci et al. 2013; Mulukutla et al. 2017). The aforementioned techniques do not form an exhaustive list of all available techniques to capture 3-D data. Readers may find other 3-D imaging techniques, including volumetric imaging such as ultrasound or magnetic resonance imaging (MRI), or other topographic imaging techniques like confocal microscopy or Moiré interferometry, that may be more suited for their application.

Regardless of chosen method to capture 3-D data, we present our work in terms of a 3-D representation of a star-like particle captured from a cloud of points depicting its exterior surface. These points, spread uniformly or randomly distributed on the surface, can be used to develop a

closed, thin-shelled polyhedron defining the surface that then can be used, if so desired, to generate a full 3D digitized representation of the object, assuming that the object is of uniform material density, since a point cloud defining the surface does not give any information about the particle's interior. The surface polyhedron consists of vertices, linear edges and triangular facets (Cromwell 1997) (Figures 5 and 6). This object is considered to be solid, with any pores on the surface considered to be part of the point cloud. Interior pores do not of course appear in a surface point cloud.

Using the above described construction, we develop a discretization of the object using different closed differential elements that are appropriate for surface area or volume calculations. The surface area of the particle can be assembled by summing up the area of the individual constituent triangular facets (A^i) of the surface. These calculations can be performed using simple geometrical formulations. With Cartesian coordinates representing the vertices $A(x_1, y_1, z_1)$, $B(x_2, y_2, z_2)$, and $C(x_3, y_3, z_3)$, the surface area of a triangular element is given as (Zwillinger 2003):

$$A_i = \frac{1}{2} |\, \overrightarrow{\boldsymbol{AB}} \times \overrightarrow{\boldsymbol{AC}} | \qquad (19)$$

where vectors $\vec{A}$,$\vec{B}$ and $\vec{C}$ are vectors formed by each side of the triangle:

$$\overrightarrow{\boldsymbol{AB}} = (x_2 - x_1)\,\hat{\imath} + (y_2 - y_1)\hat{\jmath} + (z_2 - z_1)\hat{k} \qquad (20a)$$

$$\overrightarrow{\boldsymbol{AC}} = (x_3 - x_1)\,\hat{\imath} + (y_3 - y_1)\hat{\jmath} + (z_3 - z_1)\hat{k} \qquad (20b)$$

and $\hat{\imath}$, $\hat{\jmath}$,and $\hat{k}$ are unit vectors along the *x, y* and *z* axes, respectively.

For volume calculations, each triangular facet is considered to be the base of a tetrahedron that is formed with the same interior point *O* as its opposite vertex and origin (Figure 4). The volume of this tetrahedron is given as (Altshiller-Court 1964):

$$V_i = \frac{\left|\vec{\boldsymbol{a}}_{\boldsymbol{1}} \cdot \left(\vec{\boldsymbol{a}}_{\boldsymbol{2}} \times \overrightarrow{\vec{\boldsymbol{a}}_{\boldsymbol{3}}}\right)\right|}{6} \qquad (21)$$

where, $\vec{\boldsymbol{a}}_{\boldsymbol{1}}, \vec{\boldsymbol{a}}_{\boldsymbol{2}}$ and $\vec{\boldsymbol{a}}_{\boldsymbol{3}}$ are vectors connecting *O* to each vertex A, B and C, respectively:

$$\vec{\boldsymbol{a}}_{\boldsymbol{1}} = x_1\ \hat{\imath} + y_1\,\hat{\jmath} + z_1\,\hat{k} \qquad (22a)$$

$$\vec{\boldsymbol{a}}_{\mathbf{2}} = x_2\ \hat{\imath} + y_2\,\hat{\jmath} + z_2\,\hat{k} \qquad (22b)$$

$$\vec{\boldsymbol{a}}_{\mathbf{3}} = x_3\ \hat{\imath} + y_3\,\hat{\jmath} + z_3\,\hat{k} \qquad (22c)$$

The interior point O is chosen to be a point with respect to which the object is *star-like*, so that the surface area (S) and volume (V) of the object is given by the summation of individual triangular facet areas and tetrahedra volumes:

$$\mathrm{S} = \sum_{i=1}^{n} A_i \qquad (23a)$$

$$V = \sum_{i=1}^{n} V_i \qquad (23b)$$

In order to understand the distribution of space within the object and its relationship to shape, in an approach similar to Section 2.2 we use the concept of solid angle to develop the cumulative physical fraction function. In the case of a planar triangular facet depicting the surface of a polyhedron (Figure 4), the solid angle (Ω_i) subtended at O can be determined from a numerically optimized formulation (Van Oosterom and Strackee 1983),

$$\tan\left(\frac{1}{2}\Omega_i\right) = \frac{|\vec{\boldsymbol{a}}_{\mathbf{1}}\,\vec{\boldsymbol{a}}_{\mathbf{2}}\,\vec{\boldsymbol{a}}_{\mathbf{3}}|}{a_1 a_2\, a_3 \;+\; (\vec{\boldsymbol{a}}_{\mathbf{1}}\cdot\vec{\boldsymbol{a}}_{\mathbf{2}})\mathrm{a}_3 + (\vec{\boldsymbol{a}}_{\mathbf{1}}\cdot\vec{\boldsymbol{a}}_{\mathbf{3}})a_2 + (\vec{\boldsymbol{a}}_{\mathbf{2}}\cdot\vec{\boldsymbol{a}}_{\mathbf{3}})a_1} \qquad (24)$$

where Ω_i is the solid angle contributed by one constituent triangular facet of the polyhedron surface mesh. Vectors $\vec{\boldsymbol{a}}_{\mathbf{1}}$, $\vec{\boldsymbol{a}}_{\mathbf{2}}$ **and** $\vec{\boldsymbol{a}}_{\mathbf{3}}$ are the vector position of each vertex as defined in Eqs. 22a-c (Figure 4). In the numerator, $|\vec{\boldsymbol{a}}_{\mathbf{1}}\,\vec{\boldsymbol{a}}_{\mathbf{2}}\,\vec{\boldsymbol{a}}_{\mathbf{3}}|$ represents the determinant of the three vectors calculated by their scalar triple product.

With these formulations, we have shown that an individual triangular facet of a polyhedron can be used to express its surface area and the fraction of total solid angle that it subtends with an interior point as well as the volume of a tetrahedron that it forms with said point. Thus, the surface

area and volume of each constituent element of the polyhedron can be expressed as a function of the surface's contributing solid angle ($A_i = A_i(\Omega)$; $V_i = V_i(\Omega)$). The contributing solid angle from all the constituent triangles of the polyhedron mesh is given by

$$\Omega = \sum_{i=1}^{n} \Omega_i \qquad (25)$$

The definitions of physical fraction(Δ)and the cumulative functions for physical fraction, surface area and volume (CPF,CSAF and CVF) given earlier in Eq (8) and Eqs (14a-c) also apply to all star-like polyhedrons. However, there is a difference in the definition of elemental surface area and volume for those derived for convex objects (Eqs 14a-c). Individual closed differential elements chosen to develop shape curve theory for convex objects (Figure 1) were inherently cumulative, integrating surface area and volume from the previous element. The closed tetrahedral elements used for star-like objects are not inherently cumulative (Figure 4). As a result, we write Eqs (14a-c) in a form applicable to this formulation to make them explicitly cumulative and equivalent to the convex object theoretical formulations as:

$$\Delta^c = \{\Delta_1, (\Delta_1 + \Delta_2), \dots (\Delta_1 + \Delta_2 + \Delta_3 \dots + \Delta_n)\} \qquad (26a)$$

$$A^C = \frac{\{A_1, (A_1 + A_2), \dots (A_1 + A_2 + A_3 \dots + A_n)\}}{A} \qquad (26b)$$

$$V^C = \frac{\{V_1, (V_1 + V_2), \dots (V_1 + V_2 + V_3 \dots + V_n)\}}{V} \qquad (26c)$$

where the subscript *c* denotes a cumulative function. The s*hape curves,* as defined in section 2.2 are reiterated and applied to the polyhedron. One aspect of shape curves to consider is their visual appearance. In particle reconstructions where constituent triangles are not equal in area, the sorting scheme employed can affect the visual appearance of shape curves even though their lengths are unaffected regardless of scheme. In this study, *CPF* was developed by sorting for

increasing solid angle contribution of constituent triangular elements and adding them up from least to largest. This sorting scheme is employed on CSAF, and CVF to visualize the shape curves. Care must be taken that the same sorting scheme used to develop CPF is also employed for CSAF and CVF.

3.0 Results for Regular Convex and Irregular Star-shape Objects

To further explore shape curve use in shape classification we developed 3-D representations of convex regular shapes and platonic solids (summarized in Table 2). Results from 39 unique numerically generated representations of 14 types of regular and platonic shapes are discussed here, including those of a soccer ball, prolate and oblate spheroids, and right circular cylinders. In addition to regular convex shapes, we also analyzed several thousand representations of real star-shaped non-convex particulate materials in terms of spherical harmonic series, the results of which are discussed in Section 3.2.

3.1 Regular Convex Shapes

The regular and platonic shapes were numerically generated in Matlab[1] (MATLAB 2020) using internal in-built functions or *Geom3D***,** a toolbox containing a library of functions for computational geometry (Legland 2020). Where necessary, individual representations were developed from an initial skeleton containing the minimum number of vertices required to define the particle geometry. Subsequently, edges were subdivided using linear interpolation to increase the number of surface points. Two figures illustrating this process are provided in Figure S2 (supporting information). An initial sensitivity study was performed to determine the minimum number of surface points required to produce an adequate number of planar triangular facets to aid in the development of smooth and continuous *shape curve* functions. Results showed that a

[1] Certain commercial equipment, software and/or materials are identified in this paper in order to adequately specify the experimental procedure. In no case does such identification imply recommendation or endorsement by the National Institute of Standards and Technology, nor does it imply that the equipment and/or materials used are necessarily the best available for the purpose.

minimum of 1024 points were needed to ensure this (see section 4.3 for a detailed discussion). Edge subdivision was performed so as to produce at least 1024 surface points, with the final number often exceeding this by factors up to 30. Table S1 (supporting information) provides a summary of the number of surface points in each shape and material class used in this study.

Before we extract shape curves and compactness values, we investigated the role of reference origin. Shape curve theory was developed by implicitly assuming that the reference origin for each closed differential element was placed at the center of volume of the object. Since there exists a convex kernel within a star-like object that satisfies star-shape condition, in theory the reference origin can be placed anywhere within this region. So, there is a need to understand shape curves and their relationship with the origin chosen.

We performed initial analysis on two numerically generated regular shapes- a unit sphere (R=1) and a prolate spheroid with semi-major axes lengths of 1 and 2 (Figures 5 and 6). Each shape is represented by 4900 surface points from which a triangular surface mesh was generated. Numerical estimates of surface area and volume were compared with theoretical values to ensure the accuracy of numeric implementation. The prolate spheroid's theoretical surface area was approximately 21.4784 square units, whereas the numeric estimate showed a value of 21.4464 square units, a difference of -0.15 %. A similar comparison for the spheroid volume was off by -0.36 %. A numerical estimate of the sphere's surface area had an error of -0.18 % and that for the volume was off by -0.36 %. The error estimates for the total solid angle of each shape in comparison with the theoretical value was found to be less than 10^{-14} %. This very small error value is essentially round-off error, since a closed surface of a star-like particle will give a total solid angle of 4π (see Supplementary material).

Individual plots in Figure 5 and 6 show numerous surface area or volume shape curves, each generated with a different reference origin. While the generated shapes are convex, in order

to avoid points very close to the surface within the scale of noise in numerically generated models, we located select points sufficiently far from the surface to locate the reference origin. To make selections we first chose a single point on the surface at random and then extended a line joining the geometric center (center of volume) and the chosen point. The reference origin was placed at positions measuring 0 % (center of volume), 5 %, 30 %, 50 % and 70 % of the total distance of the line, starting from the center. This procedure repeated for a randomly chosen number of points on the surface (about 5 % of all surface points) to generate approximately 4900 pairs of shape curves, with each pair generated with a distinctly different reference origin. Shape curves generated with reference origin located at the center match theoretical shape curves. For a sphere, this curve is linear, whereas it is mildly non-linear for the prolate spheroid. Another notable feature is that shape curves developed from using the particle center of volume as the origin appear to have shorter arc length compared to the other shape curves, both area and volume, based on all the other origins. In Section 3.2, we will show that this also holds true for star-like shapes. We thus refine the definition of a *shape curve* developed by the functions *CPF, CSAF, CVF* (Eqs. 13a-c) as only those generated using a reference origin located at an object's center of volume. For a convex shape like a spheroid, with this narrower shape curve definition, we can assume that deviations of a shape curve from the straight-line sphere result are solely generated by the differences in the internal distribution of space with respect to a sphere. The rest of the study uses only this narrower definition of *shape curves*.

Numerical estimates of the shape curve lengths for a sphere and a spheroid (oblate spheroid with semimajor axes lengths of 2 and 1) match up well with values derived from the theory described in Section 2.2 (Table 3). For the spheroid, the surface area shape curve length was 2.2 % longer than that of a sphere, and the volume shape curve length was 4.2 % longer than for the sphere. The corresponding differences from a sphere was 7.2 % for the sphericity and 29.2 % for the Corey

Shape Factor. These results indicate that shape curves integrate surface area and volume differently compared to single factor measures like sphericity and CSF.

A comparison of shape curves generated for 10 shapes is shown in Figures 7a-b. This provides a window into the potential use of shape curves in shape classification. Objects selected here were based on clear distinctions in perceived shape so that the shape curves were also distinct. The appearance of the shape curve for a right circular cylinder is distinct from that of all the other shapes shown in Figure 2.

Table 2 summarizes compactness values calculated for various regular and platonic shapes. Corresponding sphericity values are also provided for comparison. These compactness values are also plotted in compactness space (L_s-L_v) (Figure 8) with an illustration of select shapes. Compactness of equi-dimensional shapes cluster closely with a sphere, along the line with slope = 1, while more oblate or prolate spheroids, cylindrical or disk shapes fall farther away from this line. Volume shape curve lengths are consistently higher than the corresponding surface area shape curves. This analysis demonstrates that shape information is well integrated into shape curves and thus they can provide a basis for shape classification, including irregular star-like shapes.

3.2 Case Study-Shape Classification of Irregular Star-Shape Objects.

Shape curve analysis was performed on several thousand cement and sand particles (Table 4 and Table S1, supporting information). Cement particles have irregular geometries dictated by their manufacturing process and have been shown to generally comply with the star-shape condition (Garboczi and Bullard 2017). Naturally weathered sand particles are often rounded and less irregular in shape than cement particles. Manufactured sand particles are derived from crushed rock and may have more angular shapes similar to cement particles. Both kinds of sand particle have been shown to fulfil the star-shape condition (Barclay and Buckingham 2009; Mollon and Zhao 2013; Garboczi and Bullard 2017).

3-D representations of cement aggregates and sand particles were reconstructed from a_{nm} data (Bullard and Garboczi 2013). The quantity a_{nm} is a complex coefficient of spherical harmonic (SPHARM) functions that approximate the surface of a 3-D object (Garboczi 2002; Bullard and Garboczi 2013). Computed from 3-D voxel data generated by XCT, a_{nm} coefficients are used to develop approximations to the function r(θ,ϕ) (Eq. 3), which per the definition developed for shape curves is the distance from the center of volume to the particle surface in a direction given by the spherical polar angles (θ,ϕ), where $0 \leq \theta \leq \pi$ and $0 \leq \phi \leq 2\pi$.

$$r(\theta,\phi) = \sum_{n=0}^{\infty} \sum_{m=-n}^{n} A_{nm} Y_{nm}(\theta,\phi)$$

$Y_{nm}(\theta,\phi)$ is the spherical harmonic (SPHARM) function with indices n and m, where $-n \leq m \leq n$,

$$Y_{nm}(\theta,\phi) = \sqrt{\frac{(2n+1)(n-m)!}{4\pi(n+m)!}} P_{nm}(cos\theta) e^{im\theta}$$

and $P_{nm}(cos\theta)$ is the associated Legendre polynomial. Custom computer code was developed using the Matlab to read a_{nm} data, with n≤ 30, and reconstruct each shape and compute their associated shape curves.

A sensitivity analysis showed that for each particle reconstruction a minimum of 1024 surface points (a grid consisting of 32 X 32 points in θ and ϕ,) are necessary to sufficiently resolve the shape curve functions (*CPF*, *CSAF* and *CVF*). Doing so ensured that the error in solid angle (with respect to the true value of 4π) was +0.13 % for a select cement particle (Table 4), a lower value compared to an error of +0.38 % for a numerically generated sphere. A detailed description of the results of the sensitivity analysis is provided in Section 4.3.

We developed SPHARM reconstructions with a resolution of 12,484 surface points, approximately 10 times the minimum number required based on the sensitivity analysis. For all reconstructions, a value of n=30 (the total number of spherical harmonics actually computed for these particles) was

used. The optimal value ($n < 30$) given in the particle shape database (Garboczi, 2002) keeps the total solid angle to be within 5% of 4π. Instead, we used a threshold error of 0.5 % to filter out the small percentage of particles whose total solid angle exceeded 4π. The number of particles eliminated by this threshold varied by material class and ranged from 4.9 % for MA-111 coarse sand to only 0.2 % for MA107-6 fine sand. Processing time for each particle was reasonably small (20 s to 30 s, including SPHARM reconstruction and shape curve analysis) on a personal computer with an Intel i7 CPU at 2.1 GHz with 16 GB RAM and no graphics processing unit running a 64-bit Windows 10 Pro operating system. For more complex materials that contain more pronounced surface morphological features, an initial sensitivity study may be necessary to determine an appropriate spatial resolution for particle reconstruction. A more detailed discussion of the results of sensitivity analysis is summarized in Table 4 of Section 4.3.

Surface area and volume shape curve lengths for each shape were extracted to produce two-parameter compactness values. A scatter plot of data for two cement classes, along with their separate marginal histograms for L_s and L_v , is shown in Figure 9. The cement class labels are only arbitrary names serving to identify their shape database of origin. The scatter plot provides compactness values with the vertical dashed lines placing them in the context of previously studied regular convex shapes that span from near-spherical isometric shapes to more elongated (prolate spheroidal or cylindrical) or oblate spheroidal shapes. This plot suggests that the particles in the two cement classes are very similar in their shape as captured by shape curves. Each histogram provides a distribution of percentage of particles falling in one of 45-binned classes for shape curve length. Similar histograms of shape distribution for three different classes of sand are shown in Figure 10. For the fine sand particles (MA 107), there is a significant fraction of data points clustered near the equi-dimensional (isometric) region suggesting that they are more equi-axed particles that than those for coarse sand (MA111) and Ottawa sand, which have a gap at L_s and L_v values close to 1. Scatter plots of each sand's shape curve length (compactness) values along with

shape classification data for regular shapes are given in the supporting information (Figure S3 a-e) along with a discussion of the observed patterns. These plots together provide an approach to using shape curve analysis in the interpretation of populations. In the supporting information, shape curve lengths are compared with sphericity and Corey shape factors, the results of which provide additional evidence that shape curves capture a different signature or shape than these classic measures.

For a particle whose shape is represented by a weighted sum of SPHARM, using only the a_{00} coefficient results in a sphere. Using higher n value a_{nm} coefficients modifies the shape from the previous step producing an intermediate star-like shape until the iterative process terminates at a given value of $n \leq 30$, in this case. This gradual modification of shape can be tracked on a plot like Figure 8. Figure 11 illustrates this process by tracing the evolution of shape curve lengths of five select particles, each chosen from one of the five material classes (Table 3), along with all the data for all five classes. Each path is unique to that shape, giving rise to unique pair of final compactness values for each shape. While a more in-depth analysis of this data is needed to understand shape in each material class, these results, together with others previously discussed, provide a basis for a fully quantifiable framework that captures the shape of star-like objects always using the center of volume for the particle origin.

4.0 Discussion

Shape curve functions integrate the distribution of space within the object by mapping 3-D information into 2-D curves. Such a mapping loses most of the 3D parametric series information but should retain more information than simple shape parameters contain, so are mathematically intermediate between simple shape parameters and full 3D shape re-creations. In this section, we examine shape curve invariance with respect to translation, rotation, and scale, which is an important requirement for universal applicability of any shape measure (Bribiesca 2008). Any

discussion of numerical methods implemented on digitized representations is not complete without understanding their sensitivity to measurement resolution and noise. Different measurement resolutions capture different levels of morphological features affecting surface area and volume estimates (Garboczi 2002; Zhao and Wang 2016). Since s*hape curves* incorporate all observed scales of variations that are present in the underlying 3-D data, results may be affected by noise in the data. We examine factors that affect shape curve characterization, including difficulties in accurately estimating surface area of individual particles, a common issue in 3-D characterization studies (Erdoğan 2016), and shape curve sensitivity to errors in surface area measurements, noise, and changes in spatial resolution.

4.1 Invariance to Translation, Rotation, and Scale

Invariance to translation, rotation, and scale is at the heart of a commonly understood definition of shape, which Kendall so elegantly expressed as "all the geometrical information that remains when location, scale, and rotational effects are filtered out from an object" (Kendall 1984). The key to determining a *shape curve's* invariance to translation lies in the local reference system tied to each object. For a star-like shape, the reference origin of this coordinate system can technically be placed at any point within the convex kernel. However, as discussed in the previous section, we demonstrated that consistency in encoding shape information can be achieved by placing the reference origin at the center of volume of the object (centroid of a thin shelled polyhedron of uniform density). Doing so produces minimum shape curve lengths for that object (Figures 5-6). Comparison of *compactness* across shapes is only valid when this specific condition is satisfied, regardless of any translation of the object. Since translation does not affect a change to the centroid, it ensures that *shape curves* are invariant to translation.

A shape curve's invariance to rotation can be demonstrated by examining their nature. Random rotation of the object does not change the labels of the triangular facets that form the object, only the spatial positions of their constituent vertices. Therefore, using the same ordering of triangles to

compute the cumulative shape curve functions will result in the same values of *CVF, CPF* and *CSAF*. Lastly, scale independence is built into the shape curve function with the use of normalized and dimensionless quantities (Eqs. 26a-d) so that the same cumulative shape curve functions will be generated no matter what the scale. Satisfying these conditions enables the newly formulated shape curve analysis and compactness measure to be readily applicable to star-like particles.

4.2 Issues with Surface Area Measurement

Surface area is an important and necessary measurement to generate shape curves. However, measurement of surface area for particulate materials is often a topic of controversy and confusion as results can widely vary due to internal and external pore structures, nano-scale roughness features, and complex, highly irregular geometry. We defined surface area in this study as modified geometric surface area (MGSA), given by the total surface area represented by a closed, hollow polyhedron constructed by a thin shell of scale-specific triangles (Mulukutla et al. 2017). MGSA is a modified definition of geometric surface area (GSA), which is defined by the surface area of an equivalent regular shape (usually a sphere or ellipsoid) that best fits the object (Schroeder-Pedersen et al. 1997).

GSA and MGSA are not to be confused with the physical surface area (PSA) or specific surface area (SSA) per unit mass, commonly measured by the popular gas-absorption based BET method (Brunauer et al. 1938) that for many materials can include internal pore surfaces in its estimate. For many natural materials, the PSA/SSA is known to be orders of magnitude higher than the surface area measured by other means (Papelis et al. 2003) and therefore it may not relate well with shape. For angular and more complex materials, GSA may not capture intermediate scale features that contribute to the shape. Since MGSA does not make any shape assumptions but only incorporates the given measurement data, it is as accurate as the surface area measurement method employed.

4.3 Sensitivity to Measurement Resolution and Noise

The *shape curves* analysis method assumes that the data input is free of noise from any artifact of measurement and that any uncertainties in data are minimal relative to the size of the particle and that they do not influence the perception of shape. It is important, however, to understand the sensitivity of shape curves to noise, whether incorporated during measurement or is a numerical artifact of reconstruction. For example, the SPHARM reconstructions using a_{nm} coefficient data was corrected for noisy high frequency ripples called Gibbs phenomenon (Bullard and Garboczi 2013), minimizing errors that might otherwise get incorporated into representations as small scale morphological features. In the absence of correction, such features can affect surface area and volume measurements.

To better understand sensitivity of shape curves to noise we analyzed a numerically generated unit sphere and a cement particle with varying levels of artificially generated noise added to the data. Each surface point was generated with randomized noise incorporated into it by modifying the radial coordinate as -

$$r' = r + I\,X\;\;r$$

where r is the original noise-free coordinate, X is a uniformly distributed random number in the interval $0 < X < 1$ and I is a multiplier given as $I = [1, 10^{-1}, 10^{-2}, 10^{-3}, 10^{-6}, 10^{-9}, 0]$, where I= 0 represents a shape with no added noise. Together these variables $(I\;X\;r)$ serve to create a randomized fraction of the radial coordinate that is added on as noise. Two different values of surface points, one a low value (1024) and one representing a high value (12482 points for the cement particle and 10952 points for the sphere) were used to generate the 3-D representations. The resulting spherical and cement particle representations were analyzed for error in total solid angle and shape curve lengths (Table 4). Error estimates of solid angle were determined using the true value (4π), a known number for all star-like shapes. Since we do not know the true value of

shape curve lengths for irregular star-like particles, error estimates for the cement particle were generated by comparing values from a noise-free shape at the highest resolution. Results show that the star-shape condition is violated for representations with noise on the scale of the radial coordinate (I=1). For I=0.1, , the uncertainties in shape curve lengths and total solid angle are greater than 1 % but less than 10 %. For lower noise levels, the error estimates fall below 1 % in all variables (shape curve lengths, L_s and L_v, and solid angle) for both the low value and high value of surface points. This demonstrates that cumulative functions and their application in shape curve analysis are relatively insensitive to noise.

5.0 Summary and Conclusions

The ability of a shape metric to produce a unique value for every distinct shape is an important but often-overlooked consideration for shape characterization studies. We hypothesized that a quantitative shape measure could be developed for star-shape particles by applying a fundamental principle that the shape of an object is a unique signature of its internal volume and external surface area distribution. An application of this principle led to the development of shape curve analysis as a new method to characterize 3-D particle representations, which are mathematically intermediate between simple shape parameters and full 3D shape parametric series. We produced cumulative functions of surface area and volume whose variation with cumulative solid angle was demonstrated to provide a pair of unique signatures of shape that were invariant to translation, rotation, and scale. Analysis of numerically generated regular and platonic shapes showed that description by a two-parameter *compactness* space (Ls-Lv) provides a basis for shape classification.

Compactness values for regular and irregular shapes capture the internal spatial arrangement (relative to a sphere) as expressed by surface area and volume. Furthermore, the *compactness* space (Ls- Lv space) enables a classification methodology for shapes providing unique values for regular and platonic solids. Irregular star-like particulate materials, regardless of size, have also

been shown to fit in this space, with compactness values having similar ranges to that of the regular and platonic shapes considered in this paper. Analysis of several thousand star-like cement and sand particles suggest that shapes closely clustered in L_s- L_v space have a more similar (but not exact) spatial arrangement with each other than do shapes not clustered together. This demonstrates what is intuitively observed of many particulate materials - their shapes can fall in a spectrum of qualitative description (e.g., “equi-dimensional”, “oblate”, “prolate”, “columnar”, “bladed”, ‘rod-like”). Analysis of these real particles demonstrated that a fully quantifiable shape description can be achieved in the form a pair of histograms for L_v and L_s. These shape distributions, when produced from a statistically significant population of particle shapes (such as in Figures 9 and 10), can not only provide a quantifiable shape parameterization but also an understanding of their nature in the context of regular shapes.

In conclusion, shape curve analysis is a robust and easily implementable technique to characterize the shape of star-like particles. It produces a pair of values for every distinct shape and can be used to characterize large populations of particles. This analysis method requires that the special point needed for the star-shape condition to be satisfied is the center of volume of the particle, which also serves as the origin for generating the shape curves. The developed cumulative functions integrate shape information across scales so that any star-shaped particle, even more angular and complex materials, can be studied without any changes in the methodological assumptions. The resulting pair of histograms for L_v and L_s describe shape distributions that produce full quantifiable shape parameterizations, which can be used for further research in the very active field of the science and engineering of particulate materials.

6.0 Symbols

Symbol	Description
A_n	Surface area of closed differential element
a_{nm}	Coefficient of spherical harmonic functions
A^c	Cumulative surface area function
A_i	Area of an individual triangular facet.
$\vec{a}_1, \vec{a}_2$ and $\vec{a}_3$	Vector positions of a triangular facet's vertices.
C, C_x	Two-parameter and one-parameter compactness, respectively.
CSF	Corey shape factor.
$CSAF$	Cumulative surface area function.
CPF	Cumulative physical fraction.
CVF	Cumulative volume function.
h, h_n	Height of closed differential element in shape curve theory
I	Fractional multiplier.
l_s, l_v	Surface area and volume shape curve length, respectively.
L_s, L_v	Normalized surface area and volume shape curve length, respectively.
m	index in spherical harmonic reconstruction.
N	Number of particles
n	Number of vertices on polyhedron/number of spherical harmonics.
P_{nm}	Legendre polynomial.
r, r',r_n	Radial coordinate, or radius of closed differential element.
R_c	radius of cylinder
S	Surface of a polyhedron.
S, S_i	Total surface area of object, elemental surface area.
V, Vi	Total volume of object, elemental volume.
V^c	Cumulative volume function.
x, y, z	Cartesian coordinates.
X	Normally distributed random number $0<X<1$.
Y_{nm}	spherical harmonic (SH) function.
$\theta, \emptyset$	Azimuthal and polar angles in a spherical coordinate system.
θc	Conical angle
Ψ	Sphericity.
Ω, Ω_i	Total solid angle of polyhedron, elemental solid angle.
Δ, Δ^c	Physical fraction of object and cumulative physical fraction, respectively.

Acknowledgments

GKM acknowledges partial support from University of New Hampshire's Earth Systems Research Center and US National Science Foundation (NSF) grant EAR-0838292.

References

Albanese, A., P. S. Tang, and W. C. W. Chan. 2012. The Effect of Nanoparticle Size, Shape, and Surface Chemistry on Biological Systems. Annu. Rev. Biomed. Eng. **14**: 1–16. doi:10.1146/annurev-bioeng-071811-150124

Altshiller-Court, N. 1964. Modern pure solid geometry, Chelsea Pub. Co.

Asvestas, J. S., and D. C. Englund. 1994. Computing the solid angle subtended by a planar figure. Opt. Eng. **33**: 4055–4059.

Bagheri, G., and C. Bonadonna. 2016. On the drag of freely falling non-spherical particles. Powder Technol. **301**: 526–544. doi:10.1016/j.powtec.2016.06.015

Bagheri, G. H., C. Bonadonna, I. Manzella, and P. Vonlanthen. 2015. On the characterization of size and shape of irregular particles. Powder Technol. **270**: 141–153. doi:10.1016/j.powtec.2014.10.015

Barclay, D. R., and M. J. Buckingham. 2009. On the shapes of natural sand grains. J. Geophys. Res. Solid Earth **114**: 1–12. doi:10.1029/2008JB005993

Barrett, P. J. 1980. The shape of rock particles, a critical review. Sedimentology **27**: 291–303. doi:10.1111/j.1365-3091.1980.tb01179.x

Blott, S. J., and K. Pye. 2008. Particle shape: A review and new methods of characterization and classification. Sedimentology **55**: 31–63. doi:10.1111/j.1365-3091.2007.00892.x

Boon, J. D., D. A. Evans, and H. F. Hennigar. 1982. Spectral information from fourier analysis of digitized quartz grain profiles. J. Int. Assoc. Math. Geol. **14**: 589–605. doi:10.1007/BF01033882

Bowman, E. T., K. Soga, and W. Drummond. 2001. Particle shape characterisation using Fourier descriptor analysis. Géotechnique **51**: 545–554. doi:10.1680/geot.2001.51.6.545

Bribiesca, E. 2008. An easy measure of compactness for 2D and 3D shapes. Pattern Recognit. **41**: 543–554. doi:10.1016/j.patcog.2007.06.029

Brunauer, S., P. H. Emmett, and E. Teller. 1938. Adsorption of Gases in Multimolecular Layer. J. Am. Chem. Soc. **60**: 309–319. doi:citeulike-article-id:4074706

Bullard, J. W., and E. J. Garboczi. 2013. Defining shape measures for 3D star-shaped particles: Sphericity, roundness, and dimensions. Powder Technol. **249**: 241–252. doi:10.1016/j.powtec.2013.08.015

Chung, M. K., K. J. Worsley, B. M. Nacewicz, K. M. Dalton, and R. J. Davidson. 2010. General multivariate linear modeling of surface shapes using SurfStat. Neuroimage **53**: 491–505. doi:10.1016/j.neuroimage.2010.06.032

Colucci, S., D. M. D. M. Palladino, G. K. G. K. Mulukutla, and A. A. A. Proussevitch. 2013. 3-D reconstruction of ash vesicularity: Insights into the origin of ash-rich explosive eruptions. J. Volcanol. Geotherm. Res. **255**: 98–107. doi:10.1016/j.jvolgeores.2013.02.002

Connolly, B. J., E. Loth, and C. F. Smith. 2020. Shape and drag of irregular angular particles and test dust. Powder Technol. **363**: 275–285. doi:10.1016/j.powtec.2019.12.045

Corey, A. T. 1949. Influence of shape on the fall velocity of sand grains. COLORADO AGRICULTURAL AND MECHANICAL COLLEGE.

Cromwell, P. R. 1997. Polyhedra, Cambridge University Press.

Dorf, M., and L. Hall. 2003. Solids in R^n Whose Area Is the Derivative of the Volume. Coll. Math. J. **34**: 350–358.

Erdoğan, S. T. 2016. Simple estimation of the surface area of irregular 3D particles. J. Mater. Civ. Eng. **28**. doi:10.1061/(ASCE)MT.1943-5533.0001575

Garboczi, E. J. 2002. Three-dimensional mathematical analysis of particle shape using X-ray tomography and spherical harmonics : Application to aggregates used in concrete. Cem. Conc. Res. **32**: 1621–1638.

Garboczi, E. J., and J. W. Bullard. 2017. 3D analytical mathematical models of random star-shape particles via a combination of X-ray computed microtomography and spherical harmonic analysis. Adv. Powder Technol. **28**: 325–339. doi:10.1016/j.apt.2016.10.014

Gualda, G. A. R., D. R. Baker, and M. Polacci. 2010. Introduction: Advances in 3D imaging and analysis of geomaterials. Geosphere **6**: 468–469. doi:10.1016/S0098-3004

Heiken, G. 1972. Morphology and petrography of volcanic ashes. Bull. Geol. Soc. Am. **83**: 1961–1988. doi:10.1130/0016-7606(1972)83[1961:MAPOVA]2.0.CO;2

Jia, X., and E. J. Garboczi. 2016. Advances in shape measurement in the digital world. Particuology **26**: 19–31. doi:10.1016/j.partic.2015.12.005

Kendall, D. G. 1984. Shape manifolds, procrustean metrics, and complex projective spaces. Bull. London Math. Soc. **16**: 81–121. doi:10.1112/blms/16.2.81

Komar, P. D., and C. E. Reimers. 1978. Grain Shape Effects on Settling Rates. J. Geol. **86**: 193–209. doi:10.1086/649674

Legland, D. 2020. Geom3D- Matlab geometry toolbox for 3D geometric computing. https://github.com/mattools/matGeom.

Leith, D. 1987. Drag on Nonspherical Objects. Aerosol Sci. Technol. **6**: 153–161. doi:10.1080/02786828708959128

Li, T., S. Li, J. Zhao, P. Lu, and L. Meng. 2012. Sphericities of non-spherical objects. Particuology **10**: 97–104. doi:10.1016/j.partic.2011.07.005

Loth, E. 2008. Drag of non-spherical solid particles of regular and irregular shape. Powder Technol. **182**: 342–353. doi:10.1016/j.powtec.2007.06.001

MATLAB. 2020. version 9.8(R2020a).

Mollon, G., and J. Zhao. 2013. Generating realistic 3D sand particles using Fourier descriptors. Granul. Matter **15**: 95–108. doi:10.1007/s10035-012-0380-x

Mollon, G., and J. Zhao. 2014. 3D generation of realistic granular samples based on random fields theory and Fourier shape descriptors. Comput. Methods Appl. Mech. Eng. **279**: 46–65. doi:10.1016/j.cma.2014.06.022

Mulukutla, G. K., K. D. Genareau, A. J. Durant, and A. A. Proussevitch. 2017. Whole object surface area and volume of partial-view 3D models. Meas. Sci. Technol. **28**. doi:10.1088/1361-6501/aa75a3

Van Oosterom, a., and J. Strackee. 1983. The Solid Angle of a Plane Triangle. IEEE Trans. Biomed.

Eng. **BME-30**: 125–126. doi:10.1109/TBME.1983.325207

Papelis, C., W. Um, C. E. Russell, and J. B. Chapman. 2003. Measuring the specific surface area of natural and manmade glasses: Effects of formation process, morphology, and particle size. Colloids Surfaces A Physicochem. Eng. Asp. **215**: 221–239. doi:10.1016/S0927-7757(02)00448-X

Pirard, E. 2012. 3D imaging of individual particles: A review. Image Anal. Stereol. **31**: 65–77. doi:10.5566/ias.v31.p65-77

Pólya, G., and G. Szegö. 1951. Isoperimetric Inequalities in Mathematical Physics. (AM-27), Princeton University Press.

Proussevitch, A. A., D. L. Sahagian, and W. D. Carlson. 2007. Statistical analysis of bubble and crystal size distributions: Application to Colorado Plateau basalts. J. Volcanol. Geotherm. Res. **164**: 112–126. doi:10.1016/j.jvolgeores.2007.04.006

Qian, Z., E. J. Garboczi, G. Ye, and E. Schlangen. 2016. Anm: a geometrical model for the composite structure of mortar and concrete using real-shape particles. Mater. Struct. Constr. doi:10.1617/s11527-014-0482-5

Riley, C. M., W. I. Rose, and G. J. S. Bluth. 2003. Quantitative shape measurements of distal volcanic ash. J. Geophys. Res. Solid Earth **108**: 8–1 to 8–15. doi:10.1029/2001JB000818

Rose, W. I., and A. J. Durant. 2009. Fine ash content of explosive eruptions. J. Volcanol. Geotherm. Res. **186**: 32–39. doi:10.1016/j.jvolgeores.2009.01.010

Rose, W. I., and A. J. Durant. 2011. Fate of volcanic ash: Aggregation and fallout. Geology **39**: 895–896. doi:10.1130/focus092011.1

Schroeder-Pedersen, A., J. Kjoeller, and B. Larsen. 1997. A comparison of calculated geometric surface area and measured BET surface area for a metal powder. ASTM J. Test. Eval. **25**: 365–369.

Smith, C. R. 1968. A Characterization of Star-Shaped Sets. Am. Math. Mon. **75**: 386.

Tafti, A. P., A. B. Kirkpatrick, Z. Alavi, H. A. Owen, and Z. Yu. 2015. Recent advances in 3D SEM surface reconstruction. Micron **78**: 54–66. doi:10.1016/j.micron.2015.07.005

Taylor, B. N., and A. Thompson. 2008. The International System of Units (SI). National Institute of Standards and Technology Special Publication 330 (2008 Edition), National Institute of Standards and Technology / U.S. Department of Commerce.

Taylor, M. A. 2002. Quantitative measures for shape and size of particles. Powder Technol. **124**: 94–100. doi:10.1016/S0032-5910(01)00476-4

Vonlanthen, P., J. Rausch, R. A. Ketcham, B. Putlitz, L. P. Baumgartner, and B. Grobéty. 2015. High-resolution 3D analyses of the shape and internal constituents of small volcanic ash particles: The contribution of {SEM} micro-computed tomography (SEM micro-CT). J. Volcanol. Geotherm. Res. **293**: 1–12. doi:http://dx.doi.org/10.1016/j.jvolgeores.2014.11.016

Wadell, H. 1932. Volume, Shape, and Roundness of Rock Particles. J. Geol. **40**: 443–451. doi:10.1086/623964

Zhao, B., and J. Wang. 2016. 3D quantitative shape analysis on form, roundness, and compactness with μCT. Powder Technol. **291**: 262–275. doi:10.1016/j.powtec.2015.12.029

Zwillinger, D. 2003. Standard Mathematical Tables and Formulae, CRC.

Table 1: Summary of surface area, volume, and solid angle formulations for differential elements of three regular shapes – prolate and oblate spheroids and right circular cylinders. Please refer to Figure 1 for a visualization of the constructed differential elements and Section 2.1 and 2.2 for a discussion of analysis and results.

Shape	**Surface Area**	**Volume**	**Solid Angle**
Prolate or Oblate Spheroid	$A_{cap} = \pi ac\left\{\frac{sin^{-1}e - sin^{-1}e_1}{e} + \frac{a}{c} - \left(1 - \frac{h}{c}\right)\sqrt{1 - e_1^2}\right\}$ Where, $e = \sqrt{1 - \frac{a^2}{c^2}}$, $e_1 = e\left(1 - \frac{h}{c}\right)$	$V_{cone} = \frac{1}{3}\pi R^2(c - h)$, Where, $R = \frac{a}{c}\sqrt{c^2 - (c - h)^2}$ $V_{cap} = \frac{\pi a^2 h^2}{3c^2}(3c - h)$	$\Omega = 2\pi\,(1 - \cos\theta_c)$ Where, $\theta = tan^{-1}\left(\frac{R}{c-h}\right)$
Right circular cylinder	$A_{cyl} = 2\pi R_c h$ where R_c is the cylinder radius	$V_{cyl} = \pi {R_c}^2 h$ $V_{cone} = \frac{1}{3}\pi {R_c}^2(c - h)$	$\Omega = 2\pi\,(1 - \cos\theta_c)$ Where, $\theta_c = tan^{-1}\left(\frac{R_c}{2(L - h)}\right)$

Table 2: Summary of compactness data for regular and platonic solids. Two-parameter compactness is indicated by (Ls, Lv). The numbers in parenthesis show how many shapes of this type were considered.

Shape (# of models)	**Compactness**		**Sphericity**
	L_s	L_v	
Smooth sphere (1)	1.0000	1.0000	1.00
Soccer Ball (1)	1.0005	1.0005	0.97
Icosahedron (1)	1.0023	1.0023	0.94
Dodecahedron (1)	1.0033	1.0033	0.91
Tetrakaidecahedron (1)	1.0038	1.0046	0.91
Rhombododecahedron (1)	1.0047	1.0047	0.90
CubeOctahedron (1)	1.0049	1.0060	0.90
Octahedron (1)	1.0136	1.0136	0.85
Cube (1)	1.0168	1.0168	0.81
Durer Polyhedron (1)	1.0218	1.0252	0.81
Tetrahedron (1)	1.0541	1.0541	0.67
Oblate Spheroids (9)	1.0207-1.1976	1.0423 -1.2384	0.42-0.91
Prolate Spheroids (9)	1.0250-1.2122	1.0425-1.2382	0.59-0.93
Right circular cylinder (10)	1.0156-1.1760	1.0348-1.2149	0.68-0.83

Table 3. Comparison of numerically derived shape curve lengths with those derived from theory.

Shape	**Theoretical shape curve lengths (l_v, l_v)**	**Numeric shape curve lengths (l_v, l_v)**
Sphere	(1.4142,1.4142)	(1.4142,1.4142)
Spheroid (a=2, b=1)	(1.4495,1.4742)	(1.4495,1.4741)

Table 4: Summary of irregular shaped sand and cement particles analyzed in this study. Labels are arbitrary to distinguish them in databases. Relevant shape measurements are summarized in Figures 6-7.

Model name	**Material**	**Number of Particles Analyzed**	**Number of Valid Models* (percentage of valid models)**
CCRL141	Cement	5000	4867 (97.3%)
CCRL 163	Cement	5000	4928 (98.5%)
C109	Ottawa Sand	2,202	2199 (99.8 %)
MA107-6	Fine sand	739	738 (99.8%)
MA111-7	Coarse sand	206	196 (95.1 %)

* Models whose total solid angle was estimated to be within 0.5 % of 4π, a nominal threshold used for accuracy. For a more detailed discussion, please refer to discussion in section 3.2

Table 4: Summary of results from sensitivity analysis. A sphere and a cement particle were reconstructed with different values of add-on noise.

Model	**Number of Surface Points**	***I***	**Solid Angle error (%)**	**L_s error %**	**L_v error %**
Sphere*	1024	1	Star-shape condition violated		
		0.1	0.382	4.468	0.575
		0.01	0.387	0.32	0.198
		0.001	0.387	0.194	0.194
		1×10^{-06}	0.387	0.194	0.194
		1×10^{-09}	0.387	0.194	0.194
		0	0.387	0.194	0.194
	10952	1	Star-shape condition violated		
		0.1	0.113	6.198	0.442
		0.01	0.091	0.822	0.049
		0.001	0.091	0.05	0.046
		1×10^{-06}	0.091	0.046	0.046
		1×10^{-09}	0.091	0.046	0.046
		0	0.091	0.046	0.046
Cement Particle**	1024	1	Star-shape condition violated		
		0.1	0.131	3.301	0.222
		0.01	0.006	0.122	-0.085
		0.001	0.001	-0.047	-0.097
		1×10^{-06}	0.001	-0.054	-0.096
		1×10^{-09}	0.001	-0.054	-0.096
		0	0.000	0.000	0.000
	12482	1	Star-shape condition violated		
		0.1	0.225	5.267	0.415
		0.01	0.006	0.570	-0.031
		0.001	0.001	-0.001	-0.034
		1×10^{-06}	0.001	-0.016	-0.034
		1×10^{-09}	0.001	-0.016	-0.034
		0	-	-	-

* Error estimates calculated by comparing with true value

** Error estimates calculated by comparing with data from noise-free (I=0) high resolution model

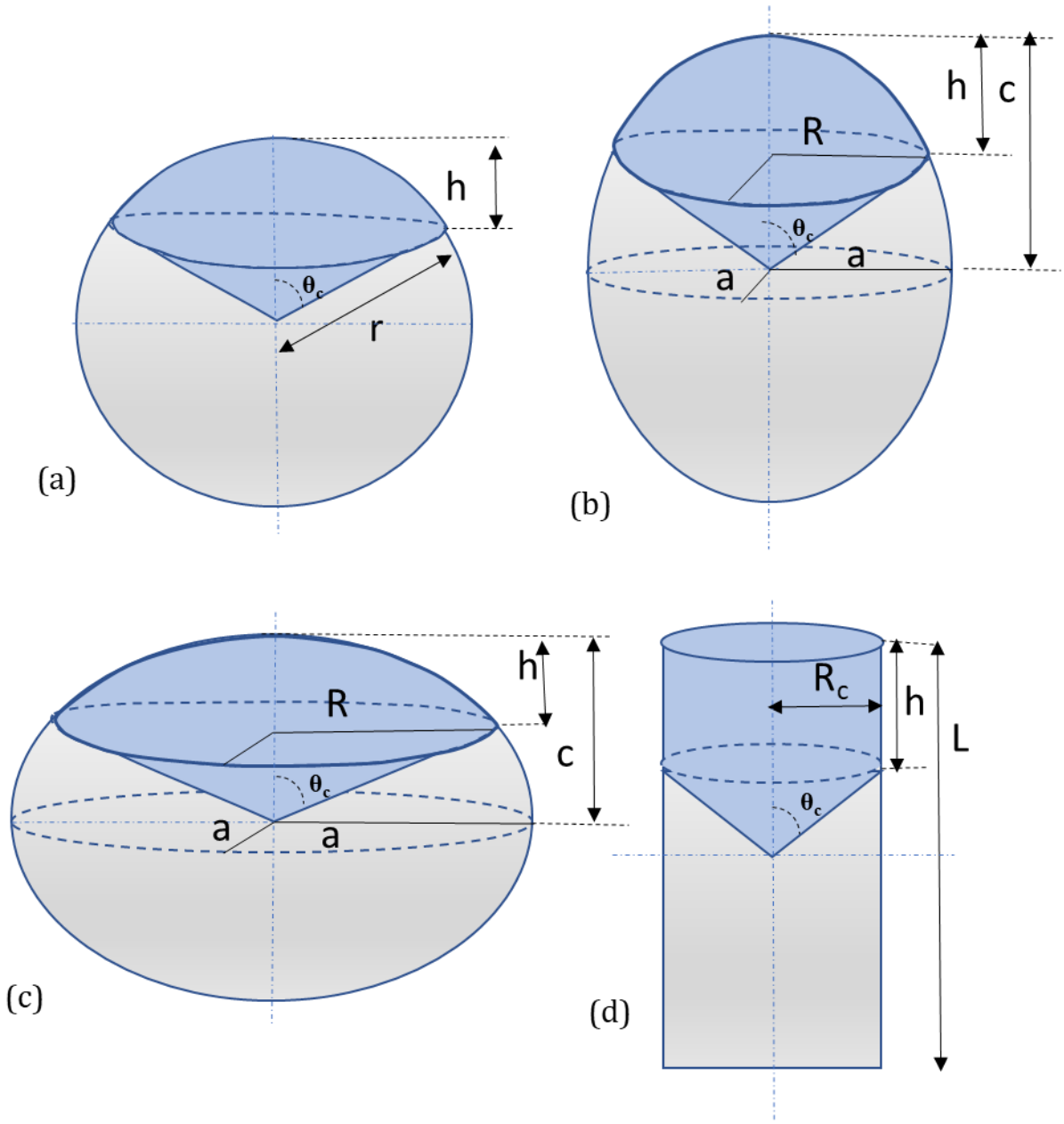

Figure 1: Differential elements shown in shaded blue color for (a) sphere (b) prolate ellipsoid (c) oblate ellipsoid (d) right circular cylinder. For surface area calculations, only the exterior facing portion of the element is considered.

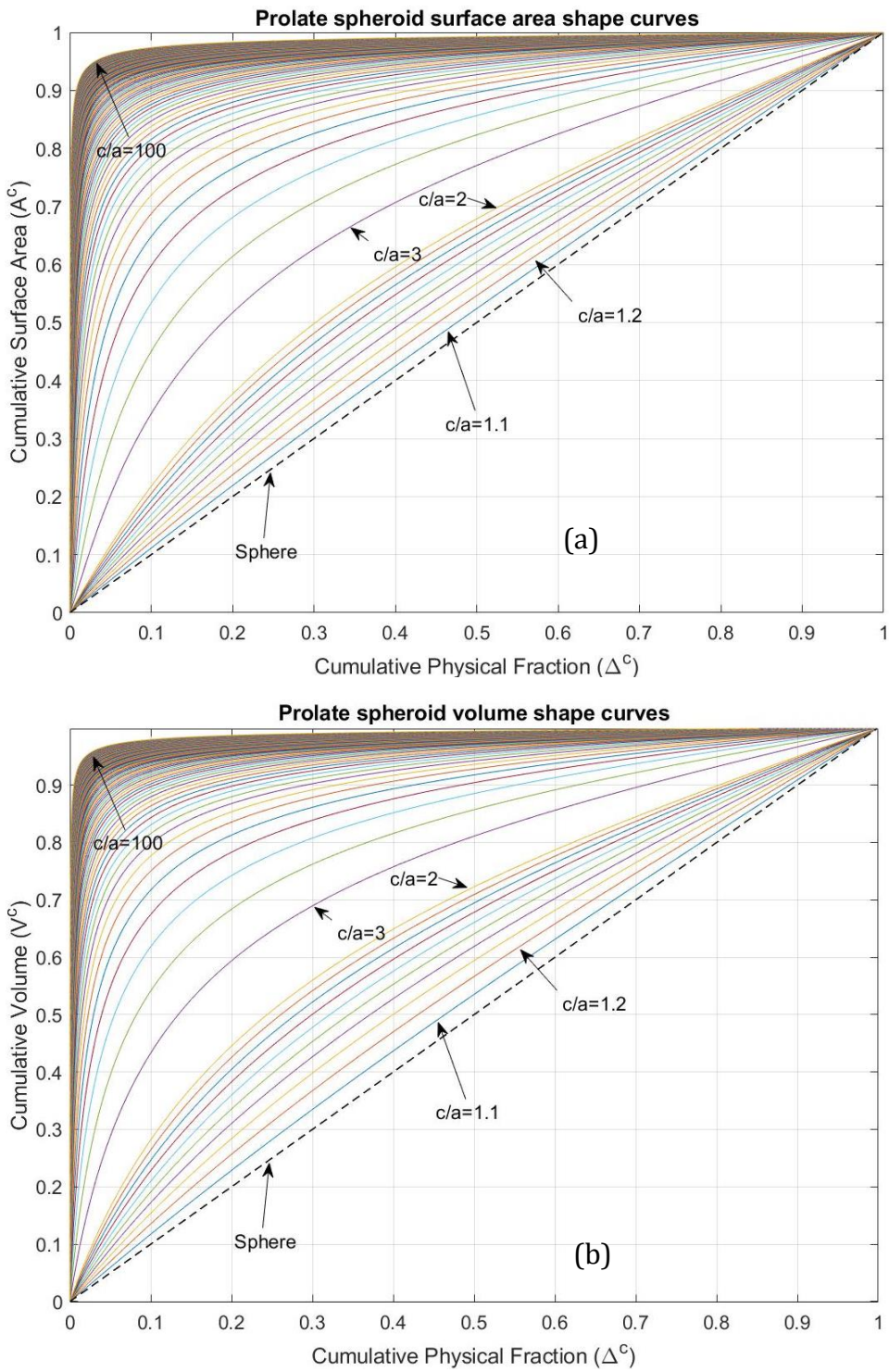

Figure 2 (a): Surface area (above) and **(b)** volume shape curves (below) for prolate spheroids. Results shown for analysis aspect ratios ranging from 1 to 100. In each plot the shape curve of a sphere (dashed line) is shown for reference. Visually perceivable differences in individual shape curves is used as a basis for shape classification.

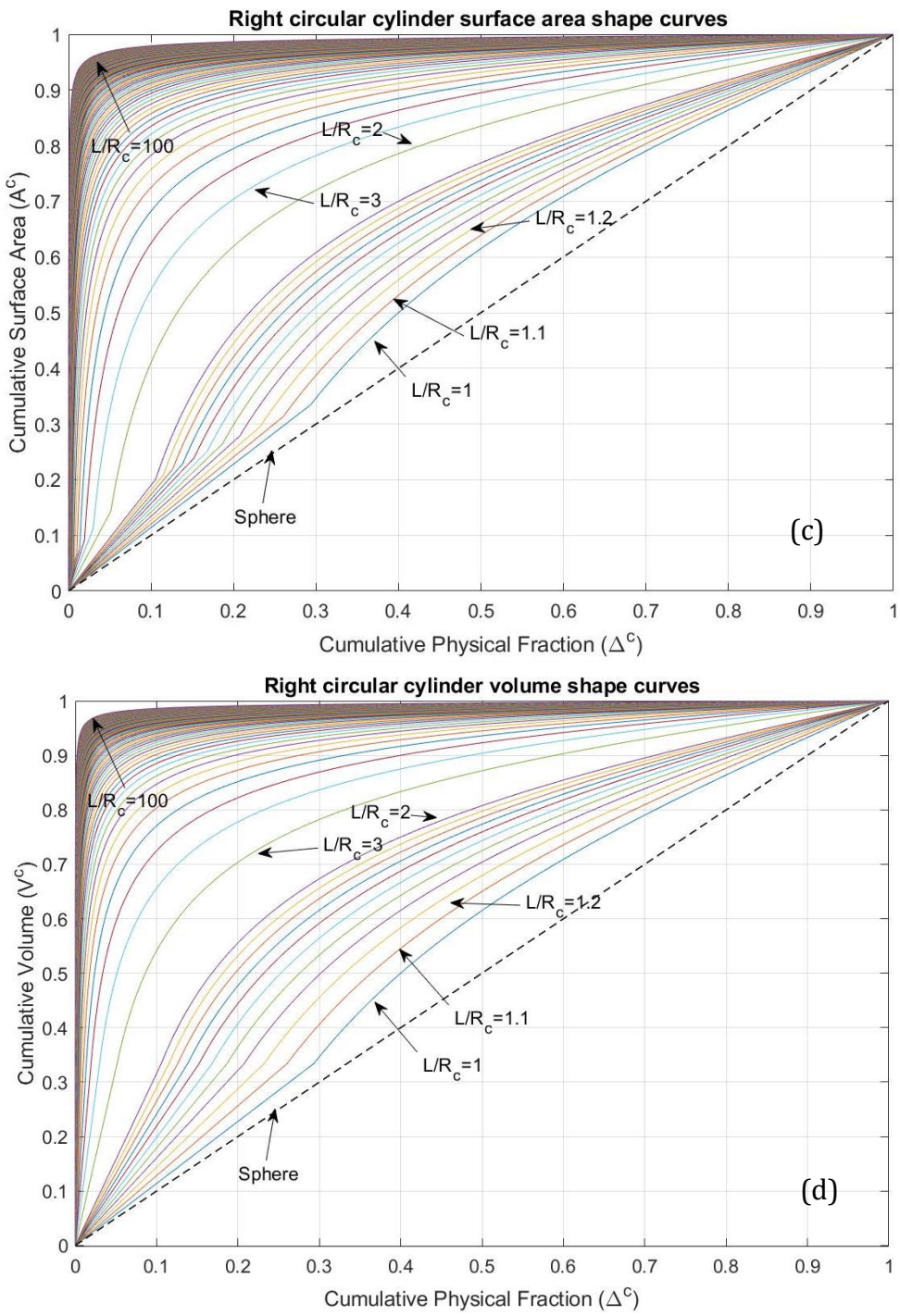

Figure 2 (c): Surface area (above) and **(d)** volume shape curves (below) for right circular cylinders. Results shown for analysis aspect ratios ranging from 1 to 100. In each plot the shape curve of a sphere is shown for reference(dashed line). Visually perceivable differences in individual shape curves is used as a basis for shape classification.

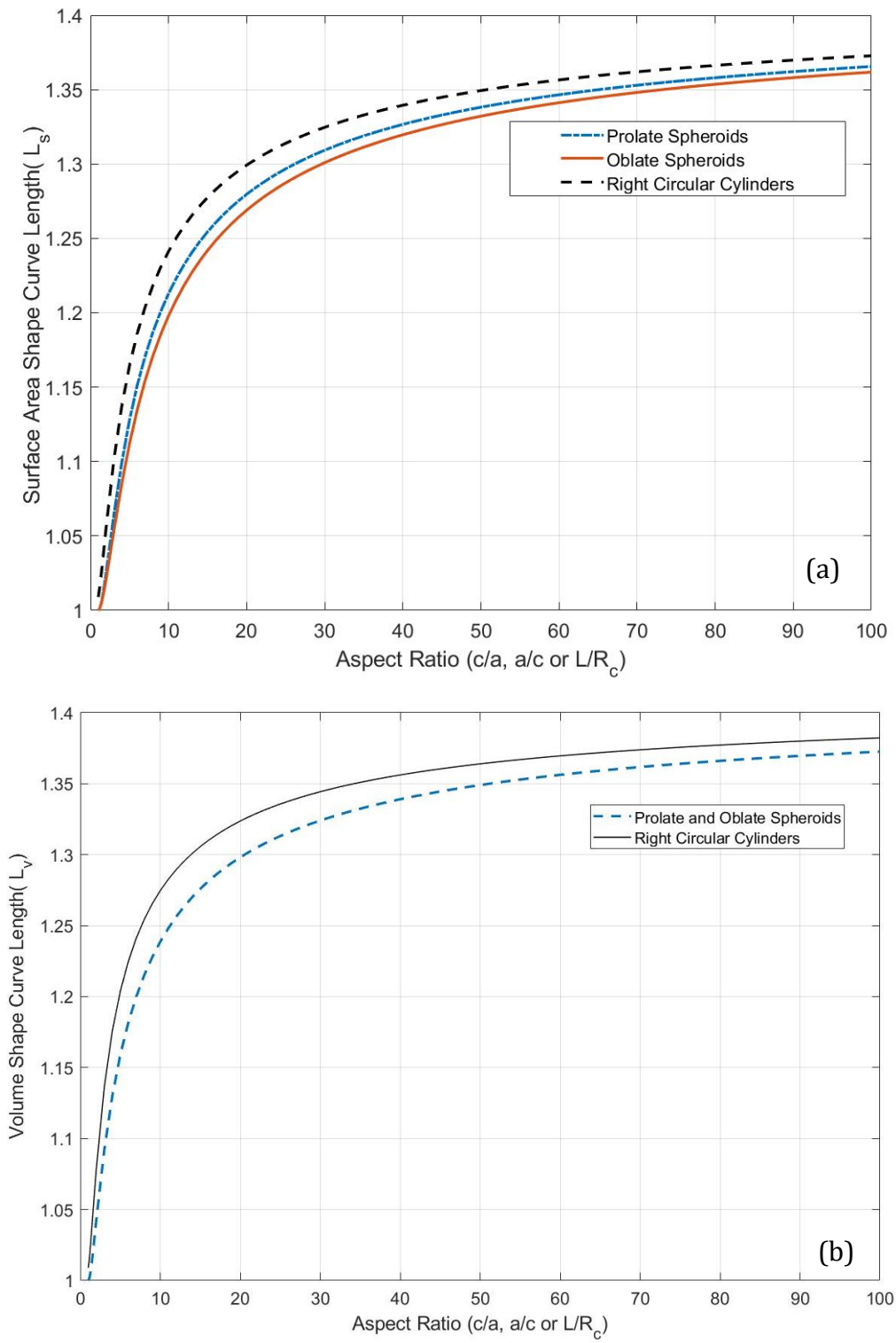

Figure 3: Analytical variation of two-parameter compactness (shape curve lengths) for prolate and oblate spheroids, and right circular cylinders of aspect ratio in the range of 1 to 100. **(a)** shows volume shape curves and (b) surface area shape curves. Compactness of a sphere is C= (1,1)

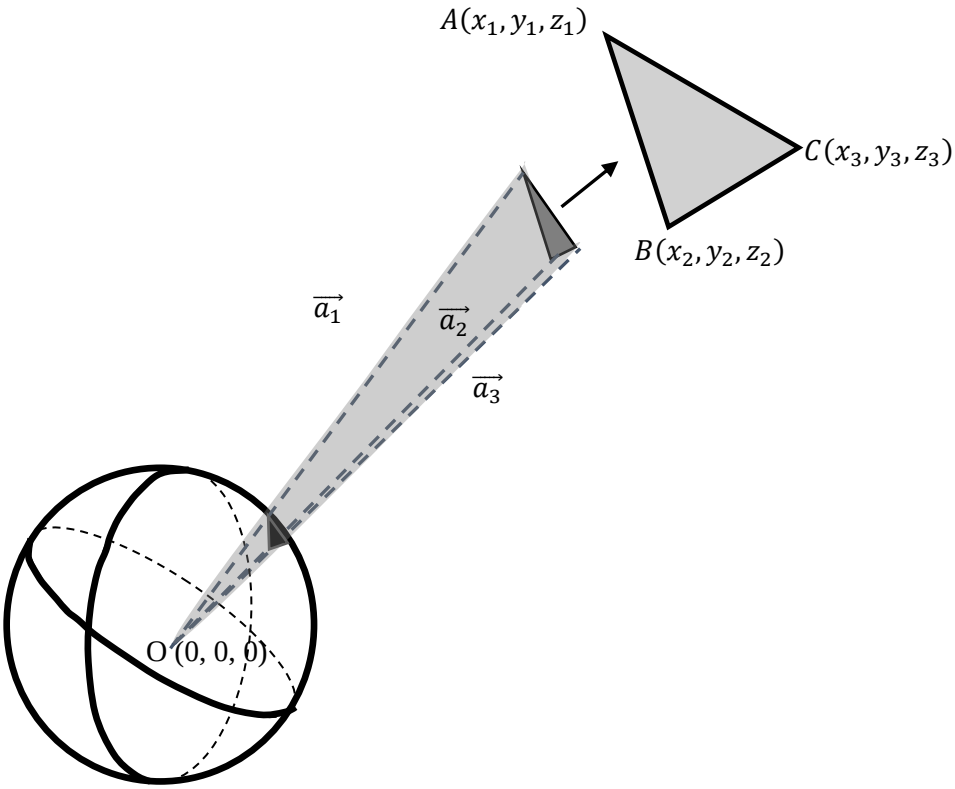

Figure 4: The solid angle of a plane triangular facet subtended at an arbitrary point O (0, 0, 0) shown as a small shaded spherical triangle on an exaggerated unit sphere. The triangular facet also forms a tetrahedron with O as the fourth vertex.

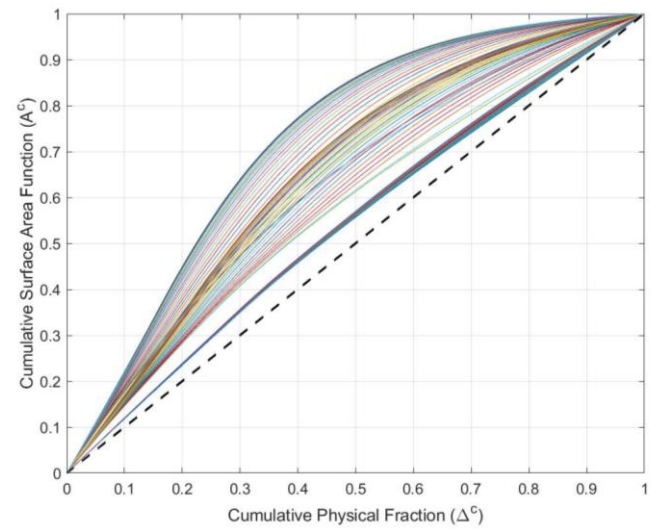

(a)

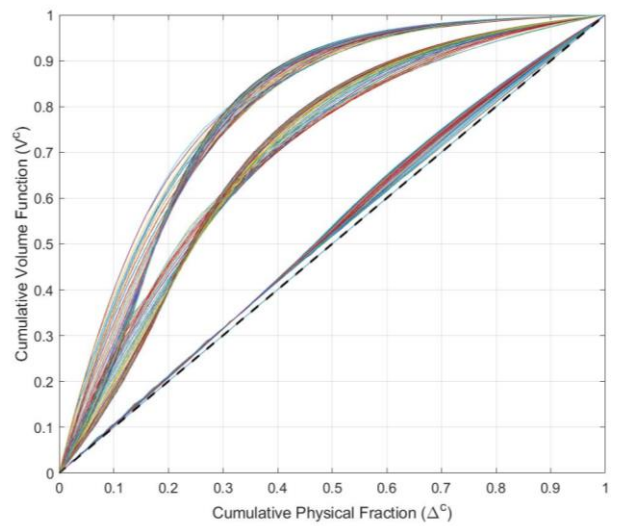

(b)

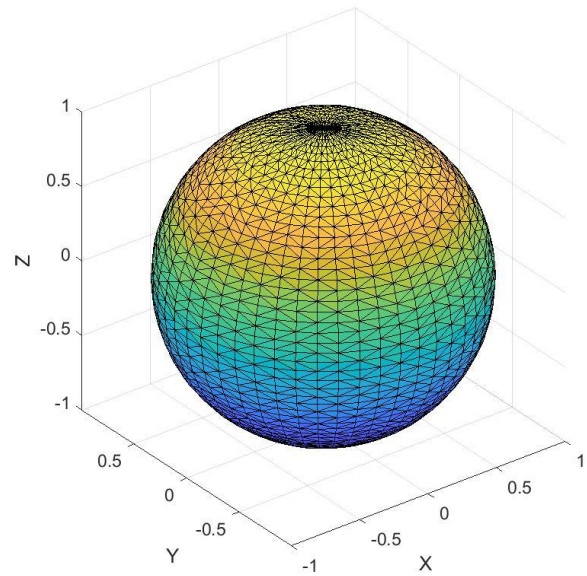

Figure 5: Shape curves of a unit radius sphere. Distribution of (a) surface area shape curves, and (b) volume shape curves. Each curve generated with select interior points located as reference origin. Shape curve generated with centroid of the sphere as reference origin are highlighted (dashed black line).

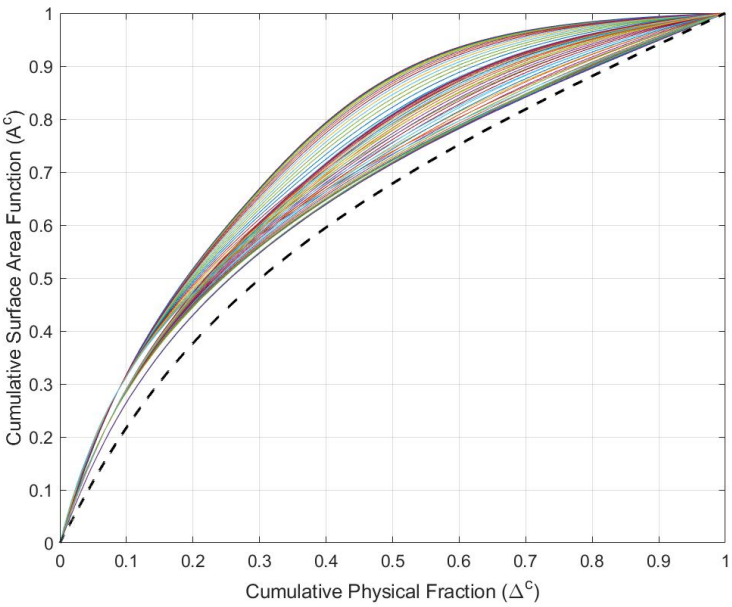

(a)

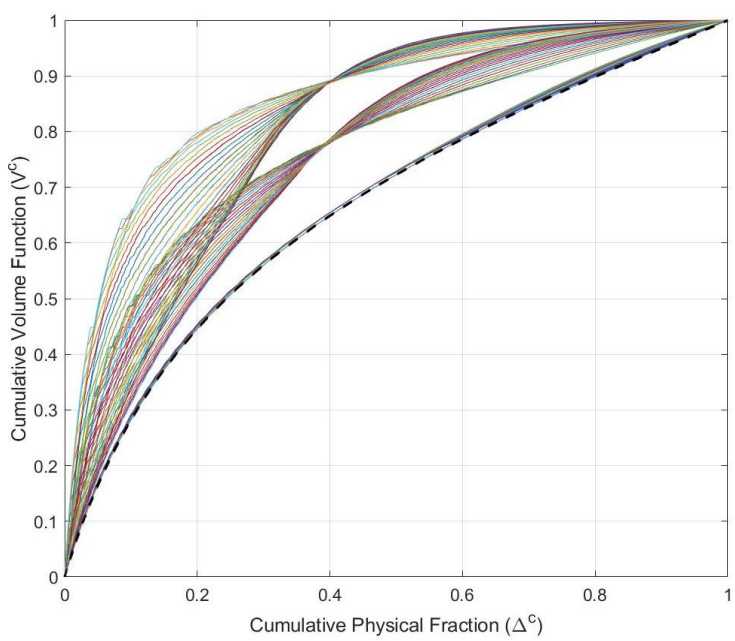

(b)

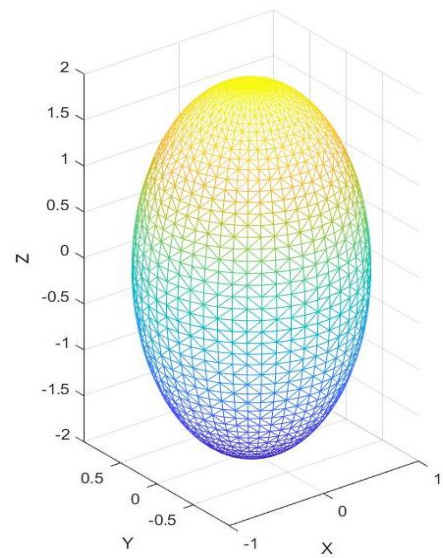

Figure 6: Shape curves of a prolate spheroid (a=1, b=1, c=2) (above). Distribution of (a) surface area shape curves, and (b) volume shape curves for select points located within the sphere. Shape curves with the center of the ellipsoid serving as the reference origin are highlighted (dashed black line).

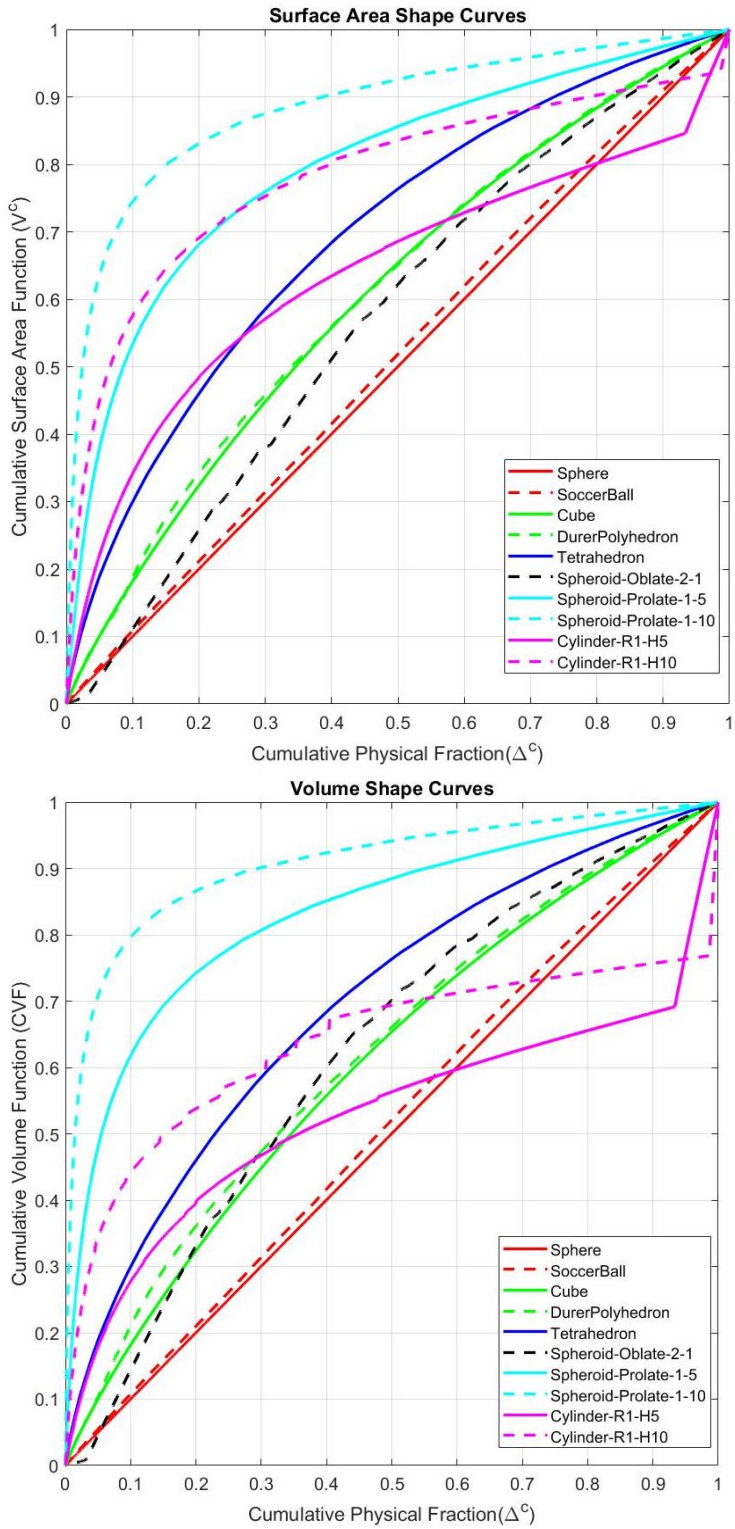

Figure 7: (above) surface area and (below) volume shape curves of select regular shapes selected to provide a contrast in shape curve lengths. Curves generated with constituent triangles sorted by their increasing contribution to total solid angle of the object.

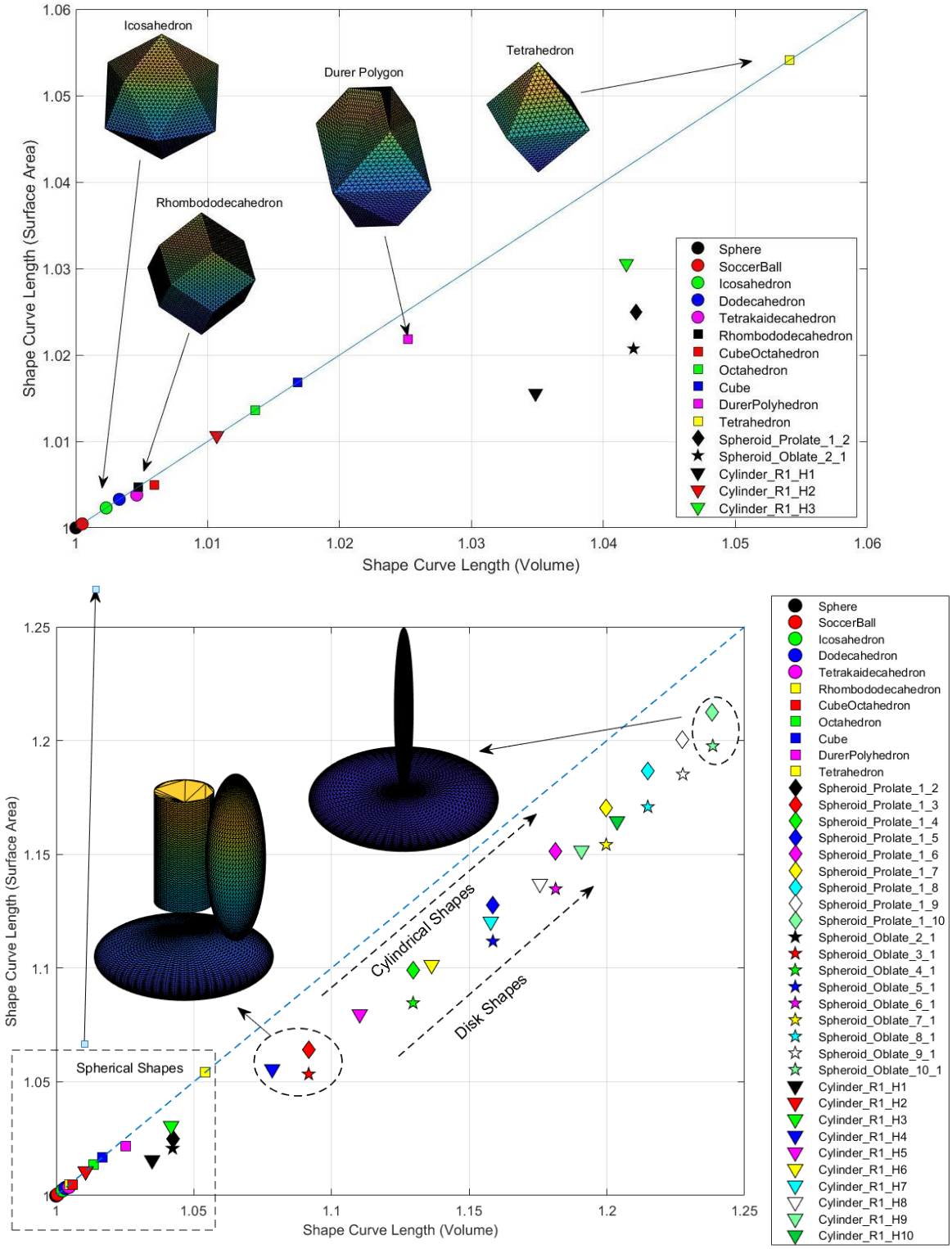

Figure 8: Plot of two-component compactness for various regular shapes (bottom). Top plot shows a zoomed-in portion of the bottom plot for near-spherical shapes.

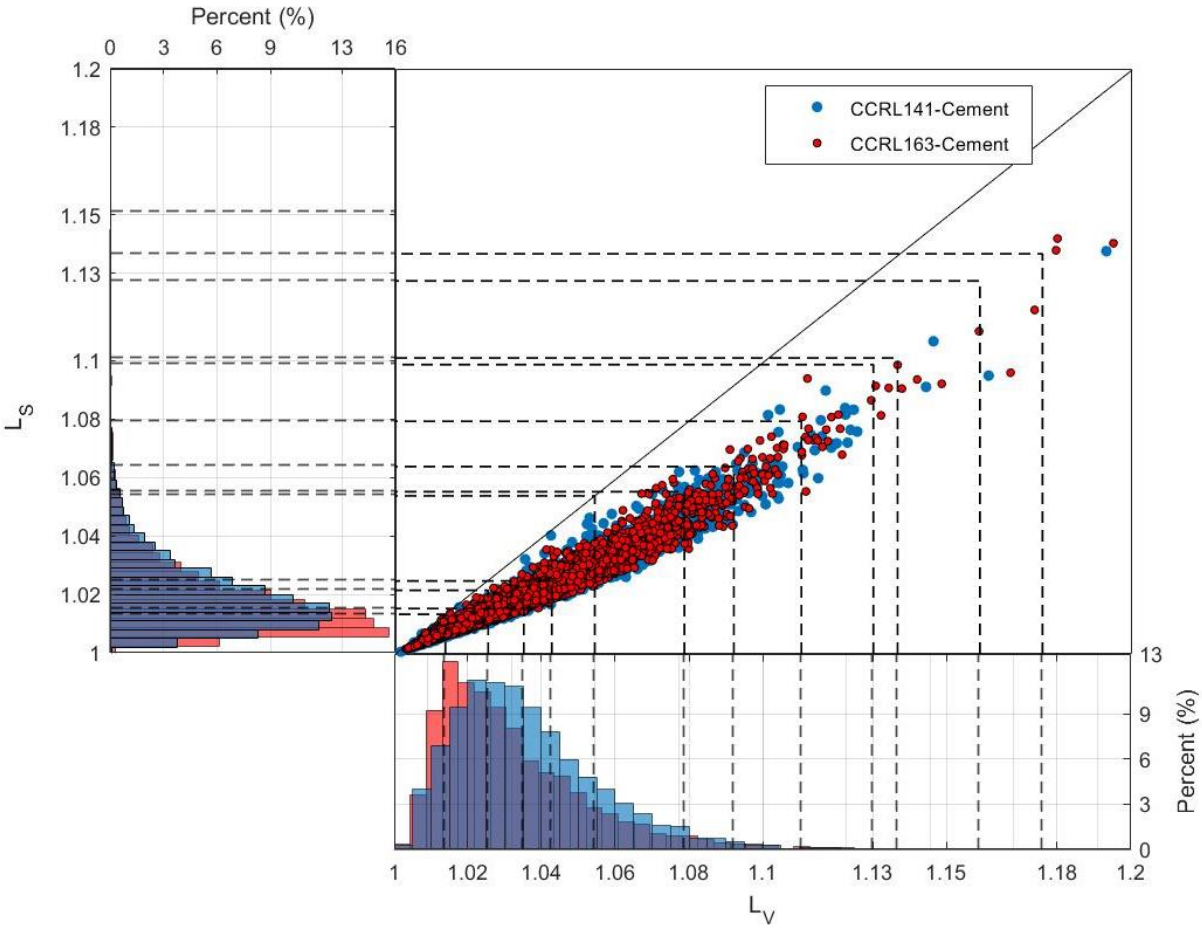

Figure 9: Scatter plot of two-parameter shape curve lengths with marginal histograms for two classes of cement particles, noted as CCRL141 and CCRL163. 5000 samples were analyzed for each class. Dotted lines show shape curve coordinates of select regular shapes shown in Figures 5. The point (L_v=1, L_s=1) represents a sphere. Like all other convex objects (regular and irregular) cement particles also fall below the line with slope 1. The L_v distribution is slightly wider than L_s. More flat and columnar shapes have increasing shape curve lengths. Each histogram contains 45 binned shape classes showing percentage of particles found in each class. Each plot has two histograms (red – CCRL 163 and blue – CCRL 141) with the intersection of the histograms shown in purple.

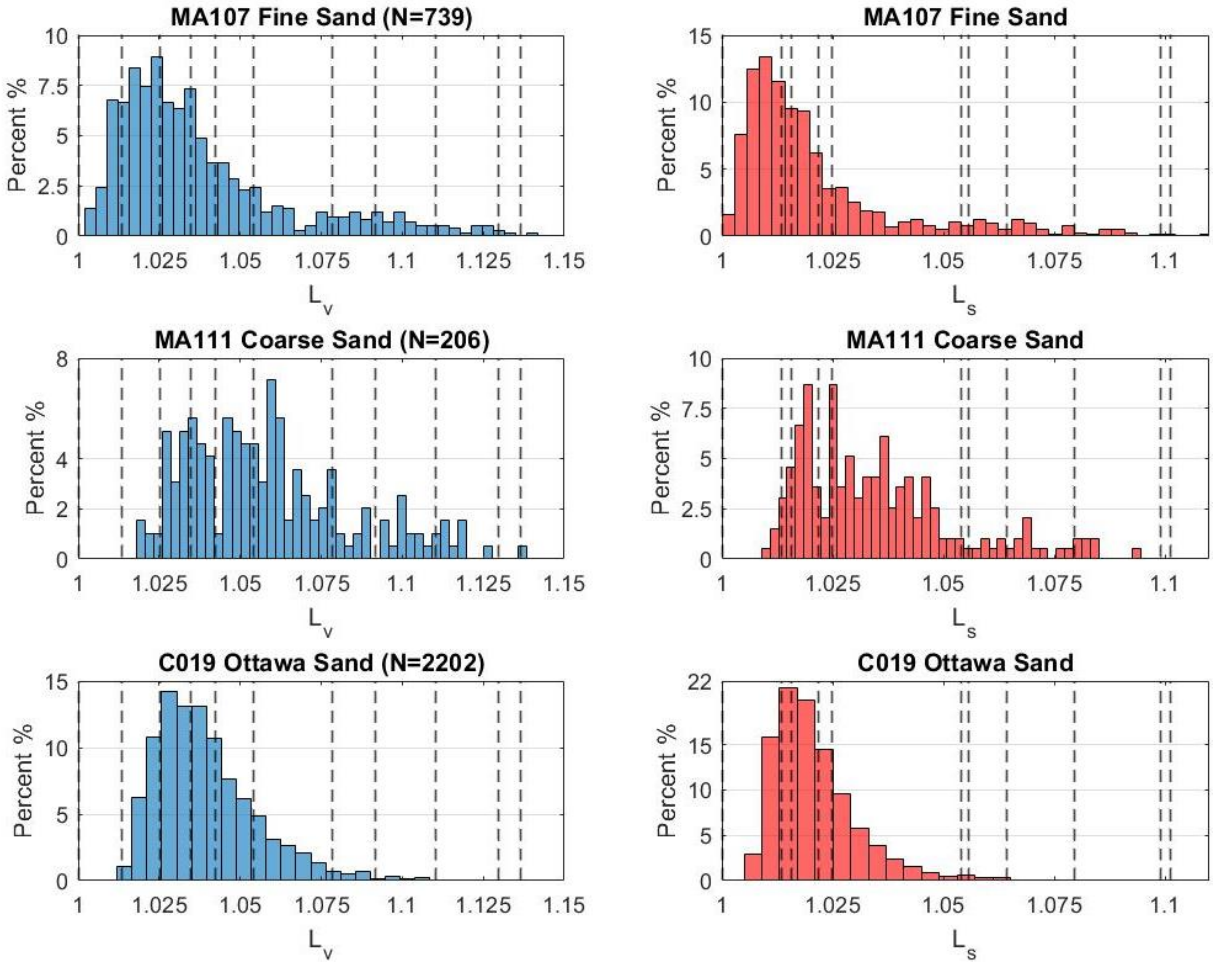

Figure 10. A compilation of shape distribution histograms of three different samples of sand. N refers to number of particle models analyzed. Dotted lines highlight shape curve coordinates of select regular shapes that were shown in Figure 8.

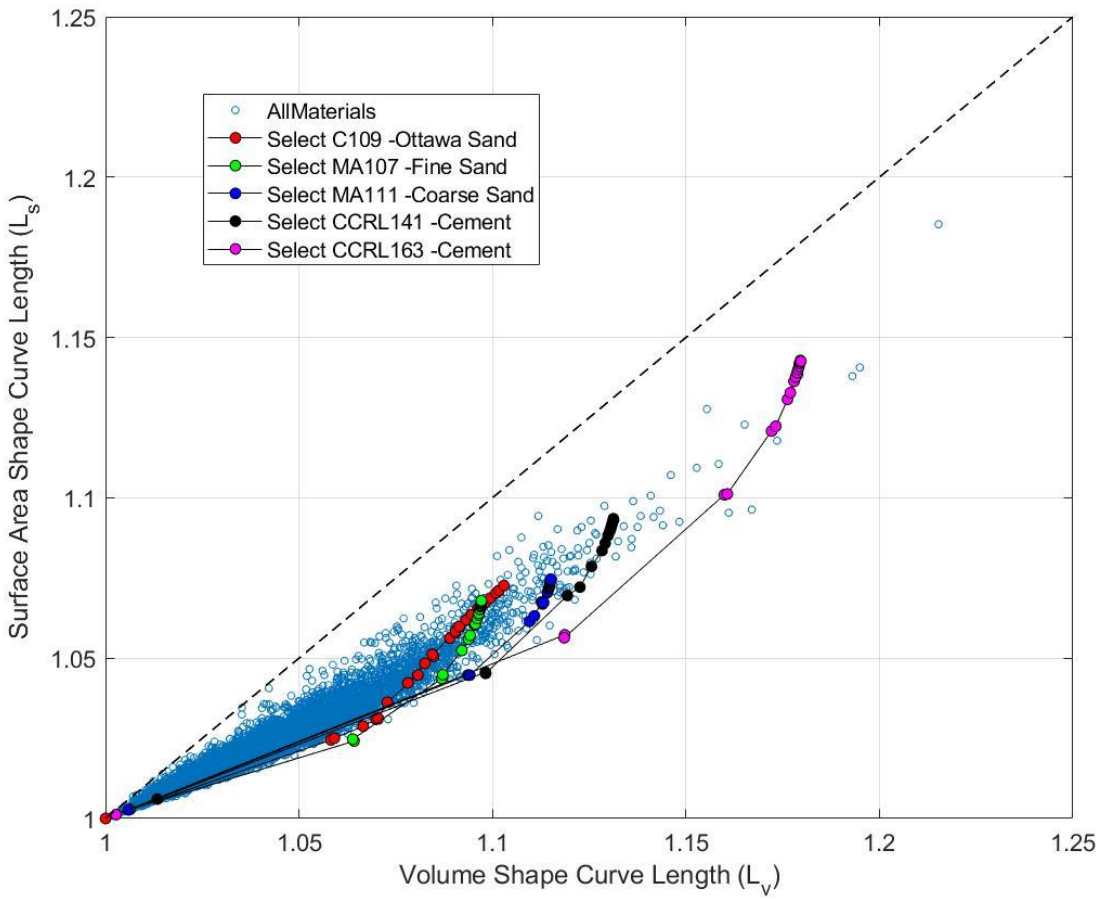

Figure 11: Evolution on shape as captured by the intermediate process steps of SPHARM. Five distinct paths are plotted each for a select model of a material class. SPHARM reconstruction begins with all shapes approximated as a sphere (Ls=1,Lv =1). Every addition of a new harmonic brings in new a_{nm} coefficients to modify the shape. Shape curve lengths for each intermediate shape is captured to create the eventual evolution of path. Final shape curve data for all materials are plotted in blue markers.

Supporting Information for

Quantifying Shape Of Star-Like Objects Using *Shape Curves* And A New Compactness Measure.

By Gopal K. Mulukutla, Emese Hadnagy, Matthew G. Fearon and Edward J. Garboczi

This document summarizes information not included in the main text.

Contents

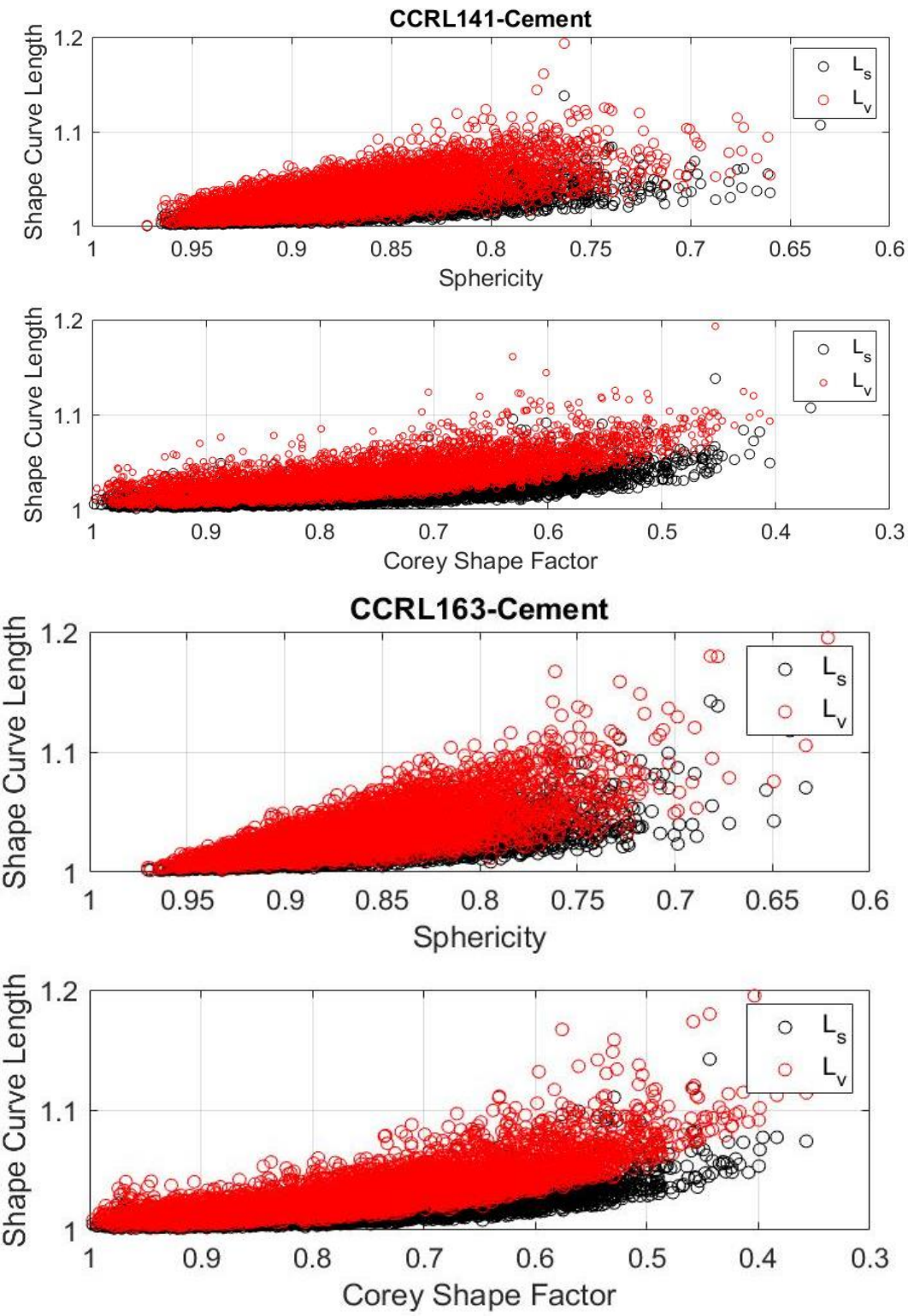
CCRL141-Cement
Shape Curve Length
Sphericity
Corey Shape Factor
CCRL163-Cement
L_s
L_v

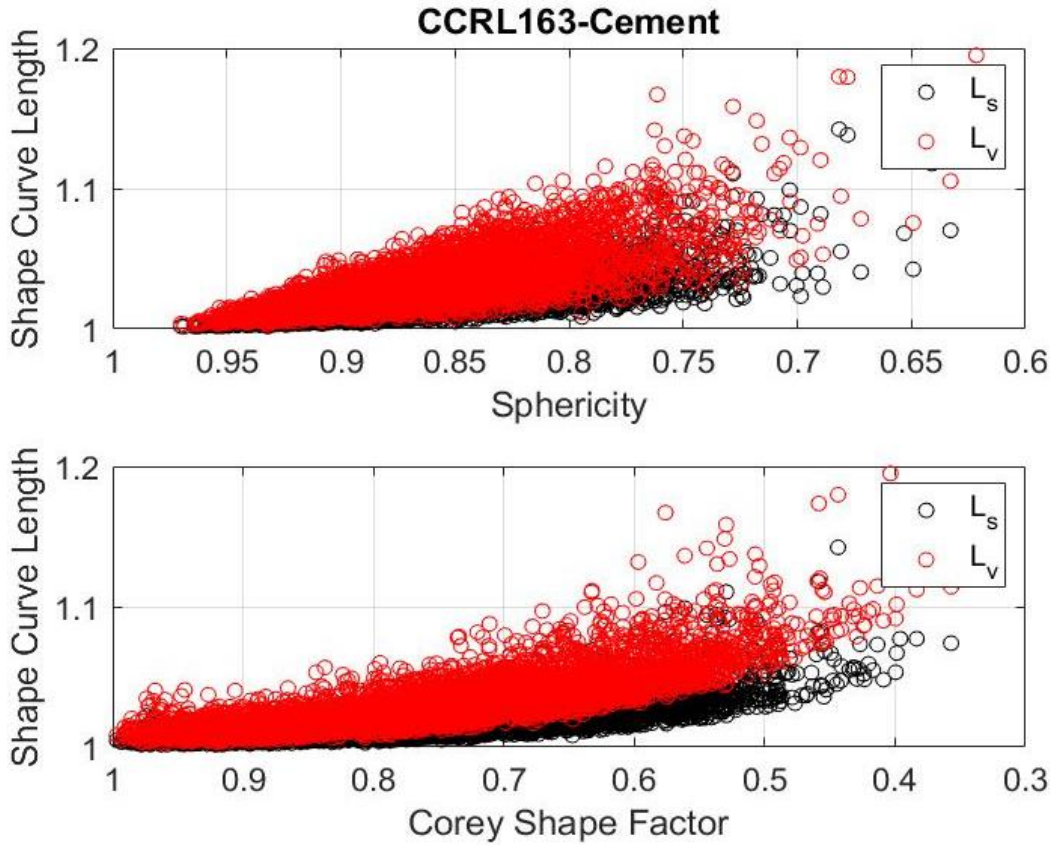
CCRL163-Cement
Shape Curve Length
Sphericity
Corey Shape Factor
L_s
L_v

16

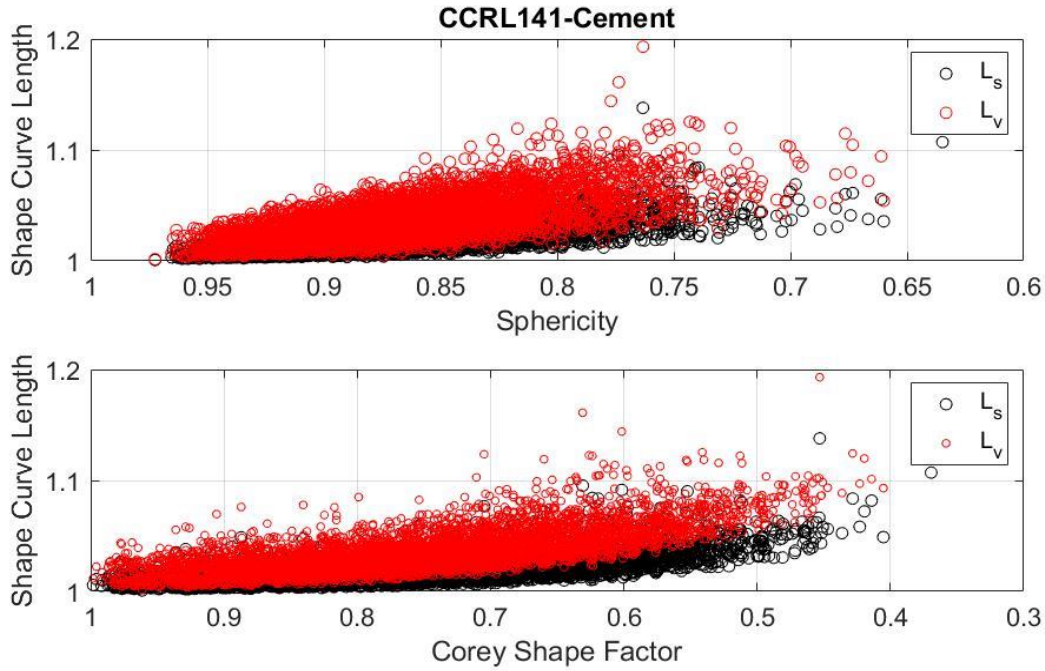
CCRL141-Cement
Shape Curve Length
Sphericity
Corey Shape Factor
L_s
L_v

16

Section S1: Solid Angle of a Star-Shape 3-D Object Subtended at an Interior Point

Consider an arbitrary star-like object depicted by a polyhedron made of equally sized elements of size dA (Figure S1). The point cloud that makes up the surface can be described in Cartesian and Spherical coordinates by Eqs (3) and (4) (Section 2.1, main text), respectively.

By definition, the solid angle $d\psi$ of a planar rectangular area in 3-D space dA at a distance r is given below, with the underlying assumption (for our case) that the reference origin is located within the interior of the object.

$$d\psi = \frac{dA}{r^2} \qquad (S1)$$

The rectangular area can be written as

$$dA = r^2 sin\theta \, d\theta \, d\phi \qquad (S2)$$

Substituting Eq (S2) in Eq (S1) gives

$$d\psi = sin\theta \, d\theta \, d\phi \qquad (S3)$$

To determine the total solid angle contributed by the polyhedron, we can develop a surface integral using Eq(S3) as shown below. The assumption of reference origin being in the interior of the object allows setting up the limits of integrations. Evaluating this integral shows the total solid angle of any star-shape object is 4π :

$$\int d\psi = \iint_S d\phi \, sin\theta \, d\theta = \int_0^{2\pi} d\phi \int_0^{\pi} sin\theta \, d\theta = 4\pi$$

Thus,

$$\psi = 4\pi$$

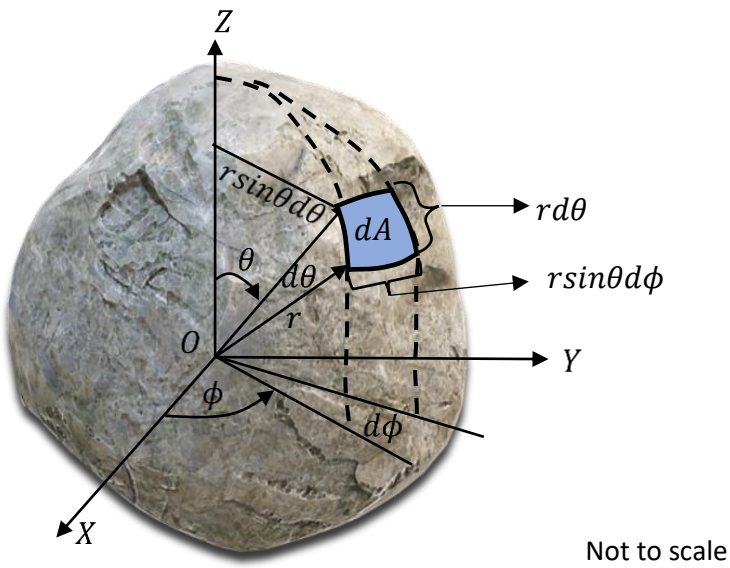

Figure S1 Showing a star-shape object, overlaid with the Cartesian coordinate system, with origin O within the interior of the object. The surface of the object is discretized into equal area planar rectangles of area dA.

Section S2: Refinement of Mesh for Regular and Platonic Solids

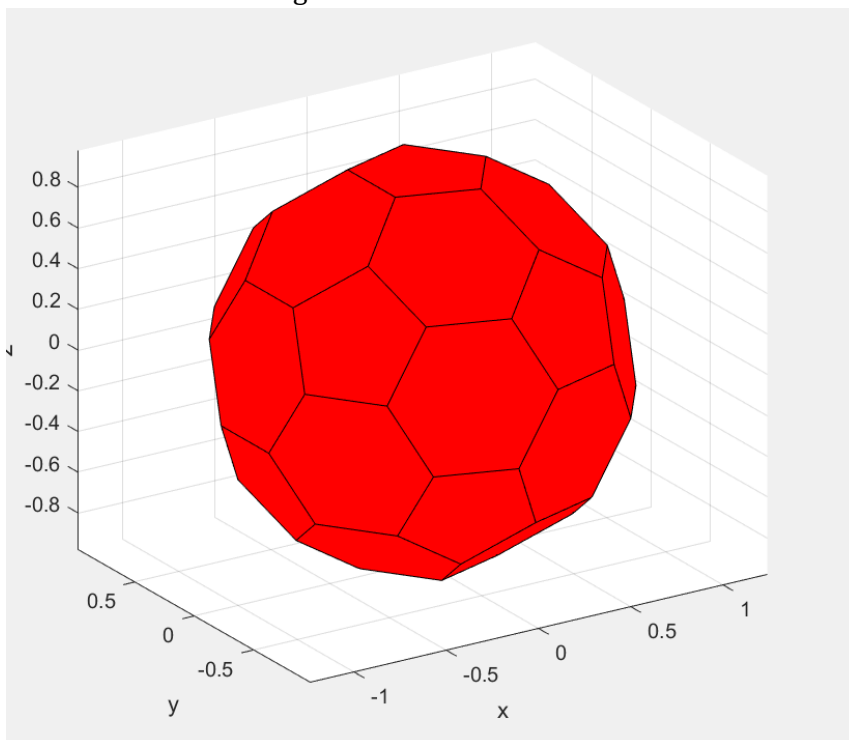

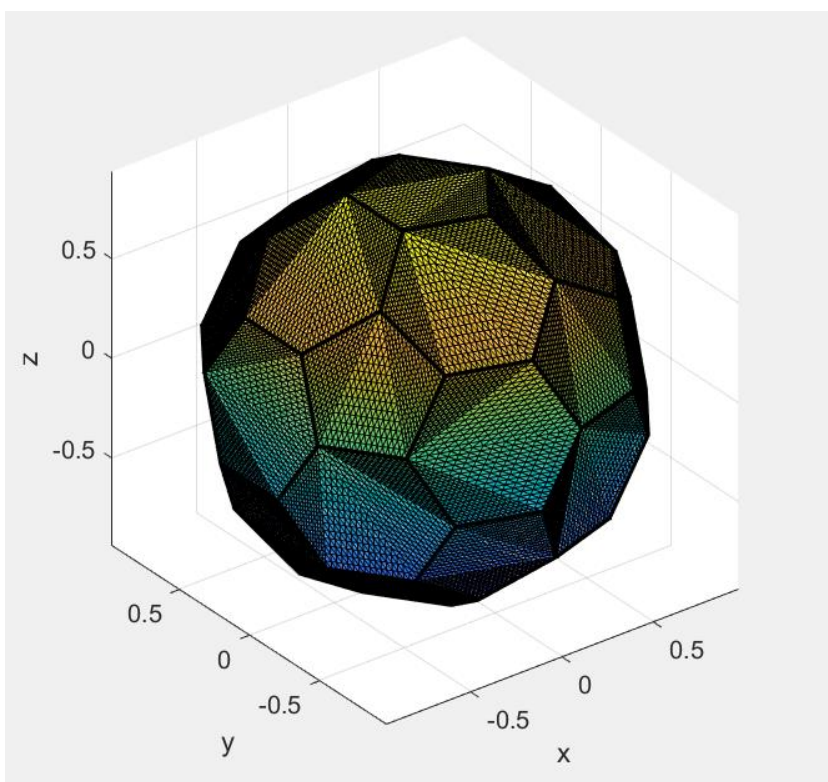

Figure S2: 3-D model of a soccer ball generated as a polyhedron (above) with the minimum number of vertices required to define shape. Each planar face is then refined with additional surface points when applying a triangulation meshing procedure.

Table S1: Characteristics of 3-D models used in this study.

Shape (# of models)	**Characteristics**
Smooth sphere (1)	7200 points-
Soccer Ball (1)	12 pentagons; 20 hexagons, 29696 pts
Icosahedron (1)	20 triangular faces, 5120 points
Dodecahedron (1)	12 pentagons, 9216 points
Tetrakaidecahedron (1)	8 hexagons, 6 squares;11264 points
Rhombododecahedron (1)	12 rhombic faces; 6144 points
CubeOctahedron (1)	8 triangles, 6 squares; 5120 points
Octahedron (1)	8 triangle faces; 2048 points
Cube (1)	4 square faces; 3072 points
Durer Polyhedron (1)	6 pentagons, 2 triangles; 5120 points
Tetrahedron (1)	4 triangle faces; 1024 points
Oblate Spheroids (9)	Semi-axes [a, c] = [2 to10,1]; 4996 points
Prolate Spheroids (9)	Semi-axes [a, c] = [1, 2 to10]; 4996 points
Right circular cylinder (10)	Two circular faces; 7200 points
CCRL141 (5000)	Cement Particles/a_{nm} models/12484 points
CCRL163 (5000)	Cement Particles/a_{nm} models/12484 points
MA107 -6 (739)	Fine sand/ a_{nm} model/12484 points
MA111 -7 (206)	Coarse sand/ a_{nm} model/12484 points
C109 (2202)	Ottawa Sand/ a_{nm} model/12484 points

Section S3: Additional Plots from Shape Curve Analysis of Irregular

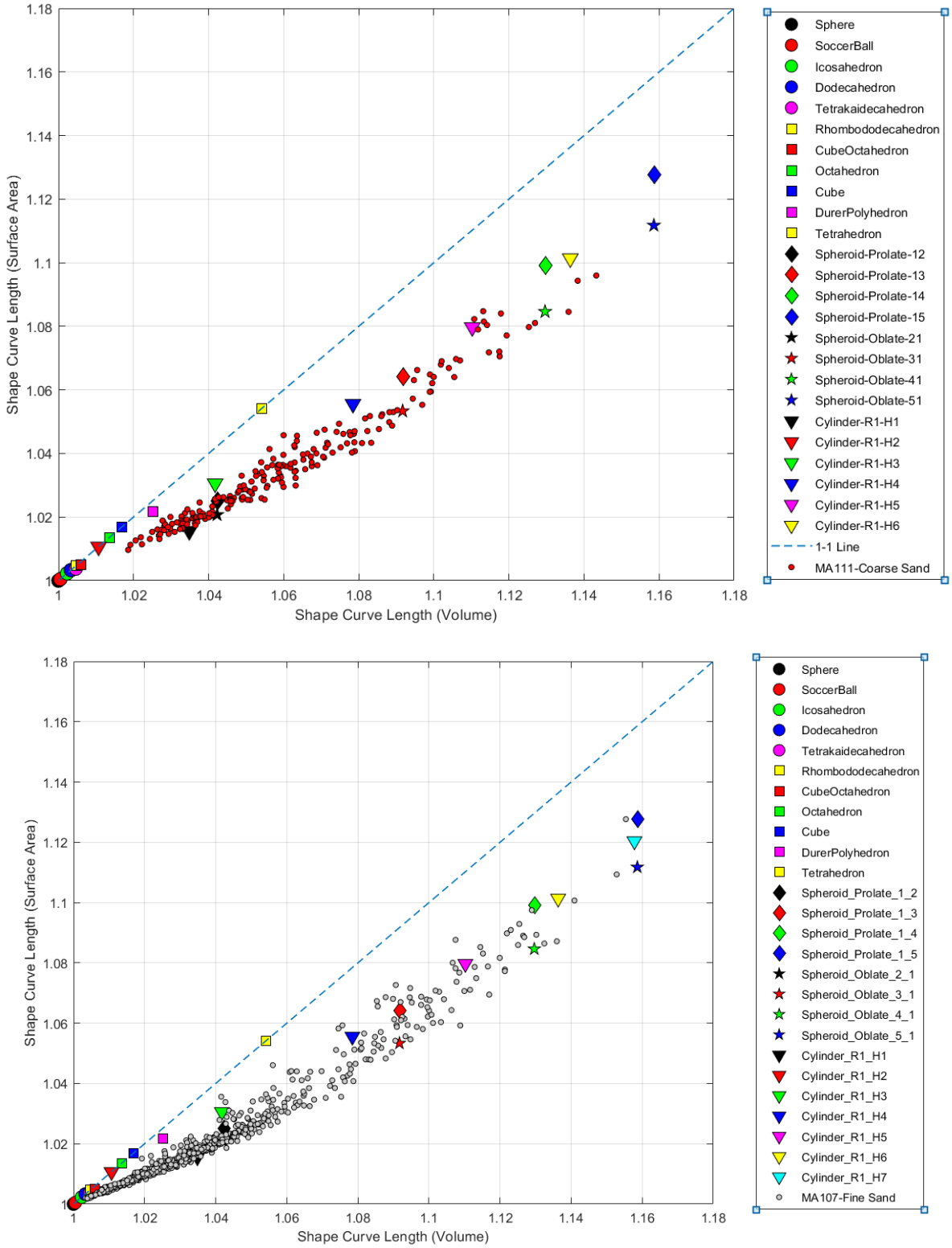

Figure S3 (a-b): Shape curve lengths of (a) MA111 coarse sand and (b) MA107 fine sand, plotted along with the data of regular and platonic solids.

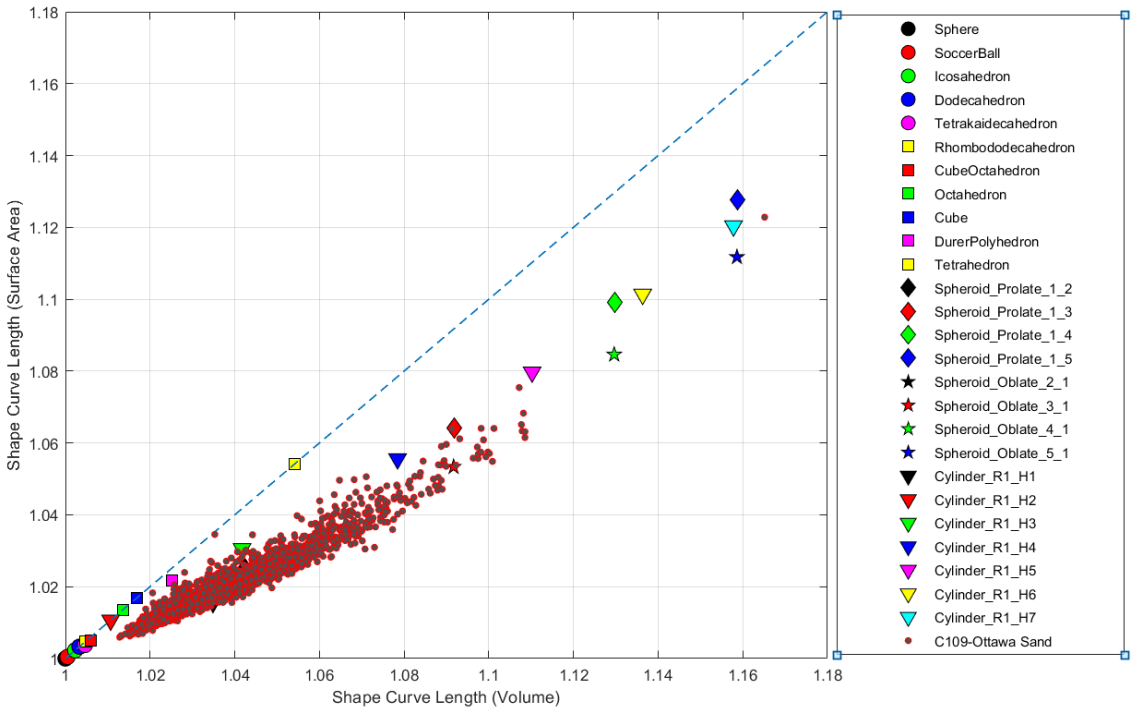

Figure S3 (c): Plot of C109 Ottawa sand shape curve lengths along with regular and platonic solids.

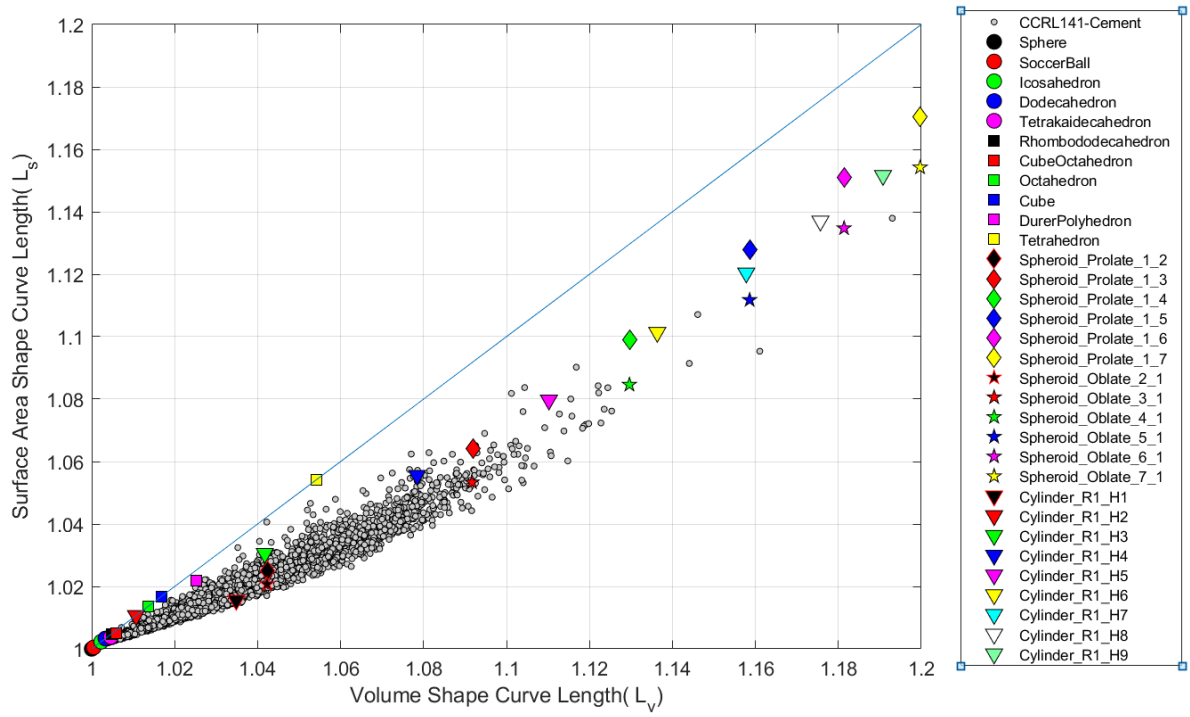

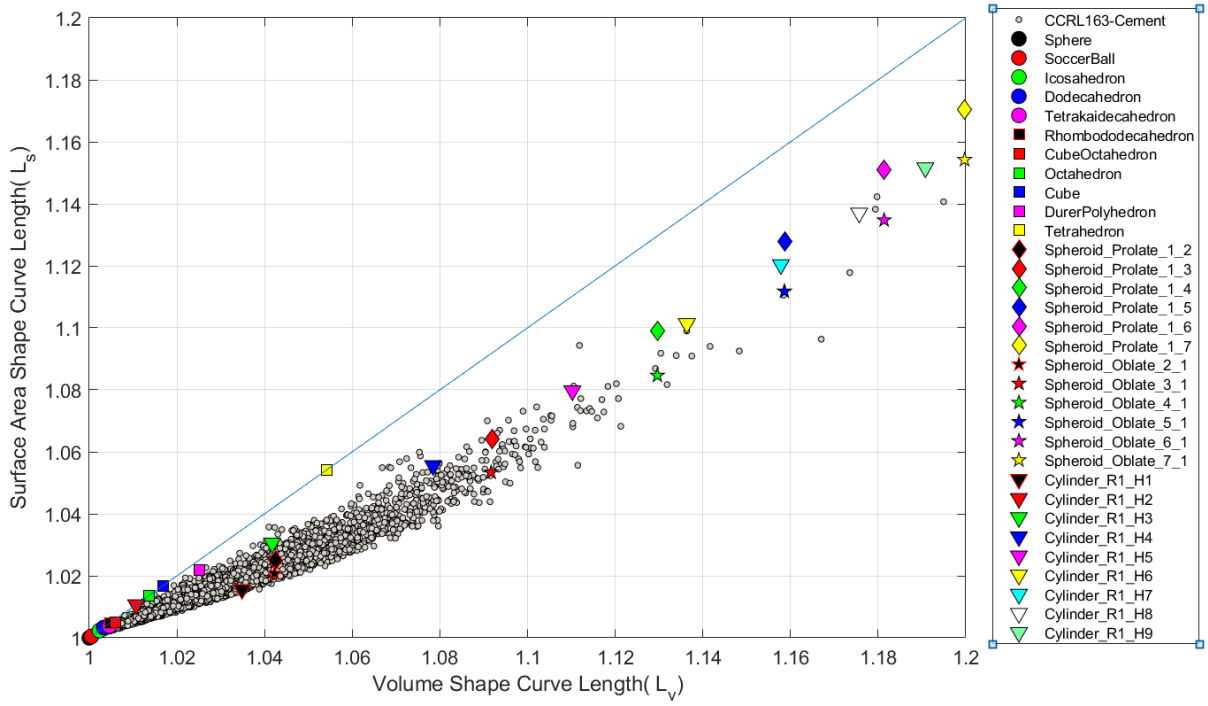

Figure S3 (d-e): Plot of shape curve lengths for cement particles (above) CCRL141 class and (below) CCRL163. Regular and platonic solid shape curve lengths are plotted for context

Section S4: Comparison of Shape Curve Data with CSF and Sphericity.

We examined the nature of shape curves in comparison with sphericity and Core Shape Factors. (CSF) (Figures S4 a-e and S5 a-e). These plots are arranged to show decreasing values in the sphericity and CSF axis with near-spherical values clustering close to lower left corner of the plots. For both cement materials (CCRL141and CCLR163) the limitation of sphericity in shape differentiation can be observed with the sparsity in values close to 1, in comparison to the presence of values for both shape curve lengths and CSF values (Figures S4 a-e). A similar observation can be made for the two sand particle classes shown in Figures S4 a-e, suggesting that sphericity is a weaker indicator of shape than CSF or shape curves. Furthermore, the slope of these relationships suggests that each shape curve captures a signature different from CSF and sphericity, and that for every unique value of shape curve length there are multiple sphericity and CSF values. By combining two such signatures, from surface area and volume shape curves, we produce a compactness measure that produce a unique pair of values for every shape. All 12942 models of irregular particles, whose compactness was captured in this study, reported a unique pair of shape curve length values. Albeit, shapes with similar arrangement of space within cluster close to each other .

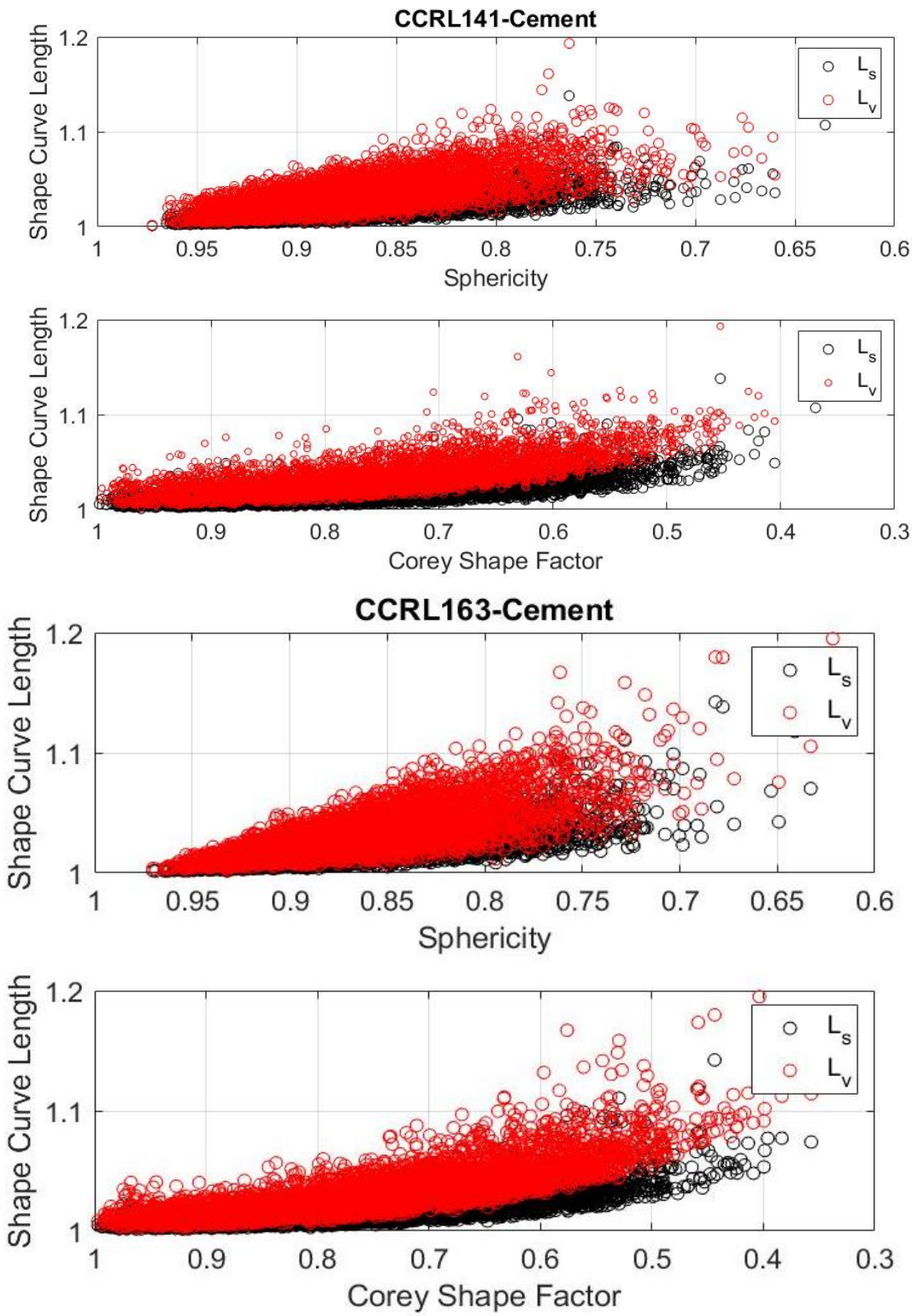

Figure S4 (a-d) Relationship of shape curve lengths to sphericity and Corey shape factor (CSF) for two cement classes. Values for CSF and Sphericity are plotted on axis with decreasing values.

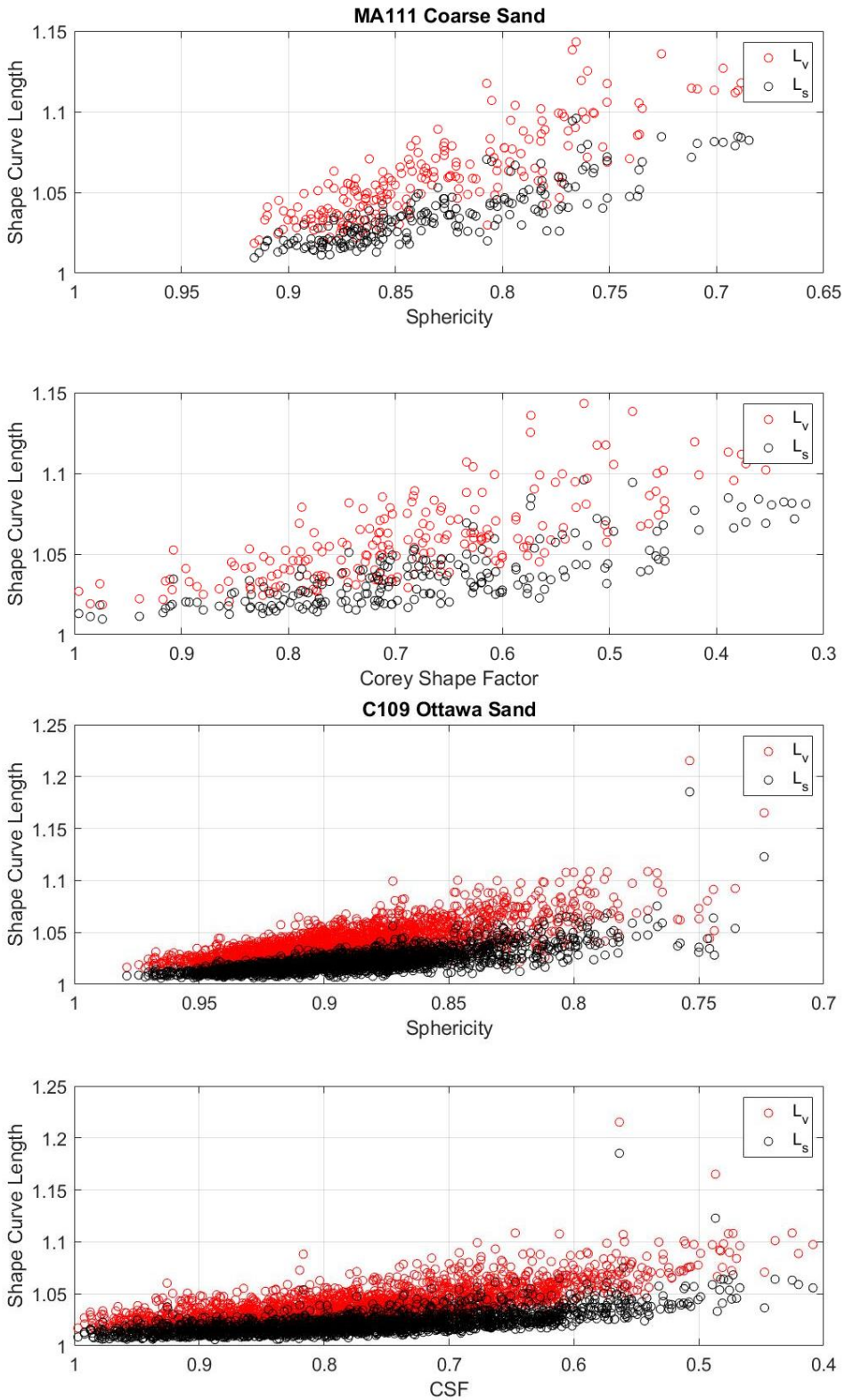

Figure S5(a-e):) Relationship of shape curve lengths to sphericity and Corey shape factor (CSF) for two sand classes (C109 Ottawa sand and MA111 coarse sand) . Values for CSF and Sphericity are plotted on axis with decreasing values.

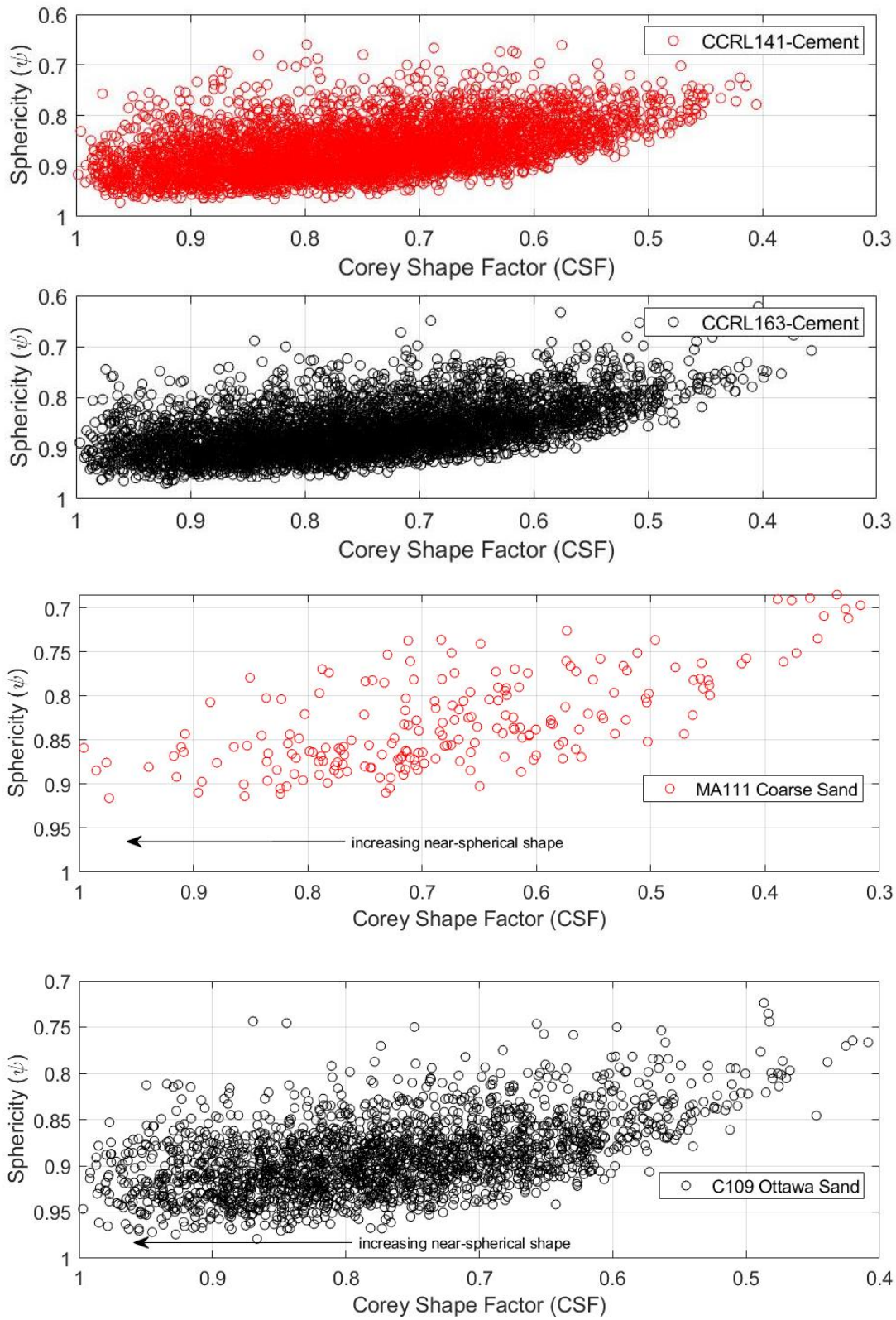

Figure S6(a-e):) Relationship of sphericity to Corey shape factor (CSF) for two cement and two sand classes. Both axes have decreasing values left to right.

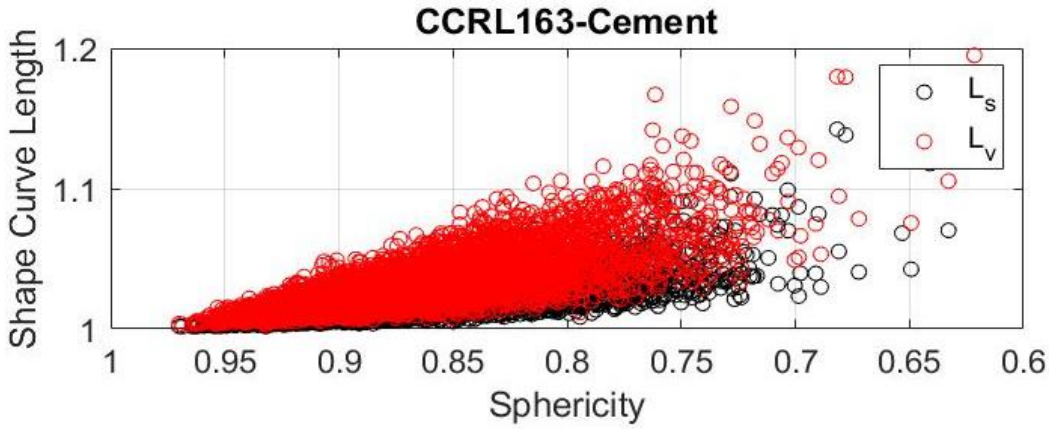
CCRL163-Cement
Shape Curve Length
1.2
1.1
1
1
0.95
0.9
0.85
0.8
0.75
0.7
0.65
0.6
Sphericity
L_s
L_v

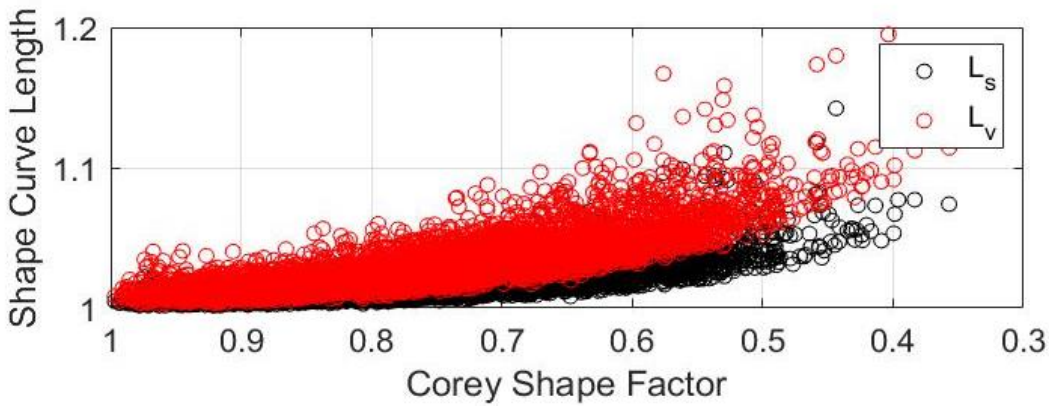
Shape Curve Length
1.2
1.1
1
1
0.9
0.8
0.7
0.6
0.5
0.4
0.3
Corey Shape Factor
L_s
L_v

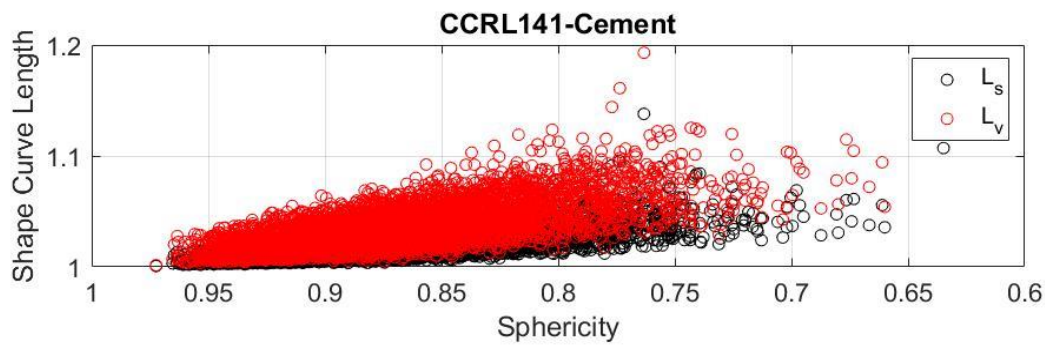
CCRL141-Cement
Shape Curve Length
1.2
1.1
1
1
0.95
0.9
0.85
0.8
0.75
0.7
0.65
0.6
Sphericity
L_s
L_v

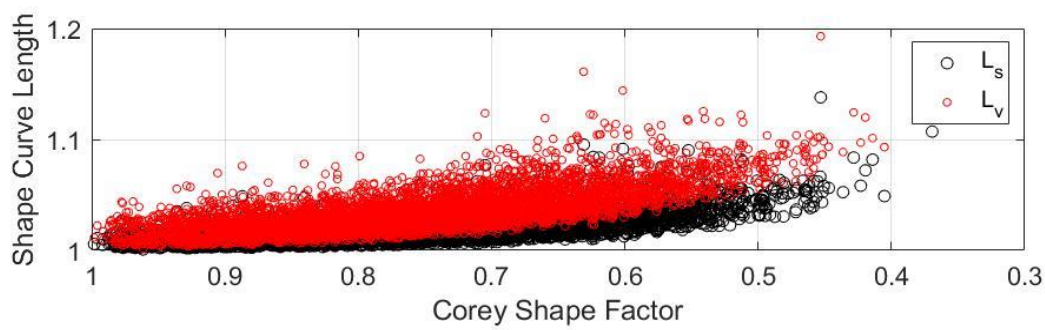
Shape Curve Length
1.2
1.1
1
1
0.9
0.8
0.7
0.6
0.5
0.4
0.3
Corey Shape Factor
L_s
L_v